# A simple disc wind model for broad absorption line quasars

N. Higginbottom,[1]★ C. Knigge,[1] K. S. Long,[2] S. A. Sim[3] and J. H. Matthews[1]

[1]*School of Physics and Astronomy, University of Southampton, Highfield, Southampton SO17 1BJ, UK*
[2]*Space Telescope Science Institute, 3700 San Martin Drive, Baltimore, MD 21218, USA*
[3]*School of Mathematics and Physics, Queens University Belfast, University Road, Belfast BT7 1NN, Northern Ireland, UK*

## ABSTRACT

Approximately 20 per cent of quasi-stellar objects (QSOs) exhibit broad, blue-shifted absorption lines in their ultraviolet spectra. Such features provide clear evidence for significant outflows from these systems, most likely in the form of accretion disc winds. These winds may represent the 'quasar' mode of feedback that is often invoked in galaxy formation/evolution models, and they are also key to unification scenarios for active galactic nuclei (AGN) and QSOs. To test these ideas, we construct a simple benchmark model of an equatorial, biconical accretion disc wind in a QSO and use a Monte Carlo ionization/radiative transfer code to calculate the ultraviolet spectra as a function of viewing angle. We find that for plausible outflow parameters, sightlines looking directly into the wind cone do produce broad, blue-shifted absorption features in the transitions typically seen in broad absorption line (BAL) QSOs. However, our benchmark model is intrinsically X-ray weak in order to prevent overionization of the outflow, and the wind does not yet produce collisionally excited line emission at the level observed in non-BAL QSOs. As a first step towards addressing these shortcomings, we discuss the sensitivity of our results to changes in the assumed X-ray luminosity and mass-loss rate, $\dot{M}_{\rm wind}$. In the context of our adopted geometry, $\dot{M}_{\rm wind} \sim \dot{M}_{\rm acc}$ is required in order to produce significant BAL features. The kinetic luminosity and momentum carried by such outflows would be sufficient to provide significant feedback.

**Key words:** radiative transfer – methods: numerical – galaxies: active – quasars: absorption lines – quasars: general.

## 1 INTRODUCTION

Outflows are key to our understanding of quasi-stellar objects (QSOs) and active galactic nuclei (AGN). First, they are ubiquitous (Kellerman et al. 1989; Ganguly & Brotherton 2008), suggesting that they are an integral part of the accretion process that fuels the central supermassive black hole (SMBH). Secondly, they can substantially alter – and in some cases dominate – the observational appearance of QSO/AGN across the entire spectral domain, from X-rays (e.g. Turner & Miller 2009), through the ultraviolet band (e.g. Weyman et al. 1991), to radio wavelengths (e.g. Begelman, Blandford & Rees 1984). Third, they represent a 'feedback' mechanism, i.e. a means by which the central engine can interact with its galactic and extragalactic environment (King 2003, 2005; Fabian 2012).

There appear to be two distinct modes of mass-loss from AGN/QSOs: (i) highly collimated relativistic jets driven from the immediate vicinity of the SMBH, (ii) slower moving, less colli-

mated, but more heavily mass-loaded outflows from the surface of the accretion disc surrounding the SMBH. Intriguingly, both types of mass-loss are also seen in other types of accreting systems on all astrophysical scales, such as young stellar objects (YSOs; e.g. Lada 1985), accreting white dwarfs in cataclysmic variables (CVs; e.g. Cordova & Mason 1982; Körding et al. 2011) and X-ray binaries containing neutron stars or stellar-mass black holes (e.g. Fender 2006; Ponti et al. 2012). Thus, the connection between accretion and mass-loss appears to be a fundamental and universal aspect of accretion physics.

Both jets and winds have been invoked as important feedback mechanisms. The current consensus (e.g. Fabian 2012) appears to be that winds may dominate feedback during bright QSO phases (the so-called 'quasar-mode' of feedback), while the kinetic power of jets may dominate during less active phases ('radio mode'). More specifically, the quasar mode may be responsible for quenching the burst of star formation that characterizes the initial growth phase of a massive galaxy, and thus for moving galaxies from the actively star-forming 'blue cloud' to the more passively evolving 'red sequence' (Granato et al. 2001; Schawinski et al. 2007). Conversely, the radio mode appears to be responsible for inhibiting new star formation

★ E-mail: nick_higginbottom@fastmail.fm

from taking place via cooling flows in massive red galaxies in the centres of clusters and groups (McNamara & Nulsen 2007).

Of the two outflow/feedback modes, jets are arguably the better understood, at least phenomenologically. Powerful jets tend to announce their presence via strong radio (and X-ray) emission, and they can often be imaged directly. By contrast, much less is known about the properties of disc winds. This is at least in part due to their much smaller physical size (e.g. Murray & Chiang 1996), which usually prevents direct imaging studies.[1] As a result, the geometry, kinematics and energetics of disc winds typically have to be inferred by indirect means (e.g. Shlosman & Vitello 1993; Knigge, Woods & Drew 1995; Arav et al. 2008; Neilsen & Lee 2009).

Arguably the most direct evidence of disc winds in AGN/QSO is provided by the class of broad absorption line quasars (BALQSOs). These objects make up $\simeq 20$ per cent of the QSO population (Knigge et al. 2008; but also see Allen et al. 2011) and exhibit broad, blue shifted absorption lines and/or P-Cygni profiles associated with strong resonance lines in the ultraviolet (UV) waveband. Such features are classic signatures of outflows and are also seen, for example, in hot stars (e.g. Morton 1967) and CVs (e.g. Greenstein & Oke 1982).

In the majority ($\gtrsim 90$ per cent) of BALQSOs, the so-called Hi-BALs, the observed absorption features are all due to relatively high-ionization species such as C IV, Si IV and N V. In a smaller ($\simeq 5$ per cent) sub-set of BALQSOs, the so-called LoBALs, blueshifted absorption is also observed in transitions associated with lower ionization species, such as Mg II and Al II. Finally, a small number ($\sim 1$ per cent) of extreme cases, the FeLoBALS, also show absorption in Fe II and Fe III.

Intriguingly, these are the same transitions that are typically seen in non-BAL QSOs and AGN, except that here they appear as pure (but still broad) emission lines. Moreover, despite differences in the continuum spectral energy distributions (SEDs), it appears that both BAL and non-BAL QSOs are drawn from the same parent population (Reichard et al. 2003). These considerations have naturally led to the suggestion that the apparent differences between BALQSOs and non-BAL QSOs are merely orientation effects (Elvis 2000). In such a geometric unification scenario, the 'broad emission line region' in non-BAL QSOs is a (possibly different) part of the same accretion disc wind that produces the absorption features in BALQSOs. The observational differences between the two classes are then solely due to viewing angle. BAL features are observed when the UV bright accretion disc is viewed through the outflow, while only BELs are seen when the system is viewed from other directions.

Given the central role played by disc winds in AGN/QSO unification scenarios and galaxy evolution models, it is clearly important to determine the physical properties – i.e. the geometry, kinematics and energetics – of these outflows. However, while there have been many previous efforts in this direction (Murray et al. 1995; Bottorff et al 1997; Everett, Königl & Karje 2001; Everett, Königl & Arav 2002; Proga & Kallman 2004; Sim 2005; Schurch & Done 2007; Schurch, Done & Proga 2009; Borguet & Hutsemékers 2010; Giustini & and Proga 2012), there has not really been a convergence towards a unique physical description. We have therefore embarked on a project to construct a comprehensive, semi-empirical picture of disc winds in AGN/QSO. Our ultimate goal is to test if outflows

can account simultaneously for most of the diverse observational tracers of disc winds in AGN/QSOs. This paper represents the first step in this long-term programme. Our aim here is to test if a simple, physically motivated disc wind model can give rise to spectra that resemble those of BALQSOs when the line of sight towards the central engine lies within the wind cone.

The detailed plan of this paper is as follows. In Section 2, we describe the family of kinematic disc wind models we use to describe AGN/QSO outflows. In Section 3, we briefly describe our Monte Carlo ionization and radiative transfer code, PYTHON (Long & Knigge 2002, LK02 hereafter), focusing on the extensions and modifications we have implemented to enable its application to AGN/QSO winds. In Section 4, we discuss observational and theoretical constraints that restrict the relevant parameter space of the model. These considerations allow us to define a benchmark disc wind model as a reasonable starting point for investigating the impact of disc winds on the spectra of AGN/QSO. In Section 5, we present and discuss the synthetic spectra produced by this model. In Section 6, we consider the main shortcomings of the benchmark model and, as a first step towards overcoming them, explore the model's sensitivity to changes in X-ray luminosity and mass outflow rate. Finally in Section 7, we summarize our findings.

## 2 THE KINEMATIC DISC WIND MODEL

Since the driving mechanism, geometry and dynamics of AGN/QSO disc winds are all highly uncertain, we use a flexible, purely kinematic model to describe the outflow. This allows us to describe a wide range of plausible disc winds within a single, simple framework. The specific prescription we use was developed by Shlosman & Vitello (1993, SV93 hereafter) to model the accretion disc winds observed in CVs, i.e. accreting white dwarf binary systems.

The geometry of our outflow model is illustrated in Fig. 1. A biconical wind is taken to emanate between radii $r_{\rm min}$ and $r_{\rm max}$ in the accretion disc, with the wind boundaries making angles of $\theta_{\rm min}$ and $\theta_{\rm max}$ with the axis of symmetry. At each radius, $r_0$, within this range, the wind leaves the disc with a poloidal (non-rotational) velocity vector oriented at an angle $\theta$ to the axis of symmetry, with $\theta$ given by

$$\theta = \theta_{\rm min} + (\theta_{\rm max} - \theta_{\rm min})\, x^{\gamma}, \tag{1}$$
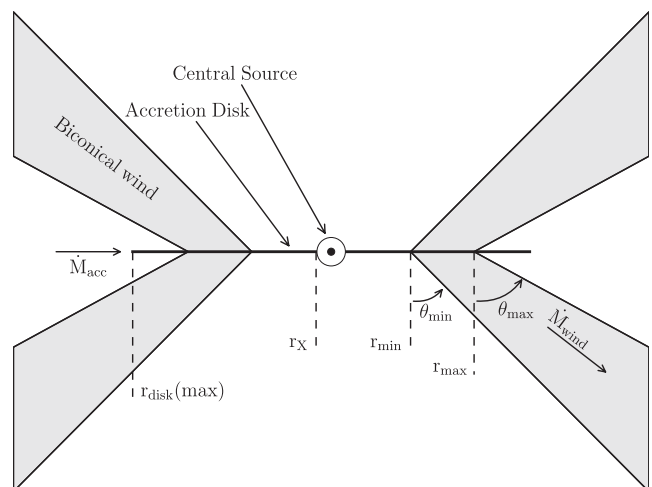


**Figure 1.** A sketch illustrating the main features of our kinematic disc wind model.

---

[1] Some disc winds in the local Universe *have* been imaged directly. For example, the spatially resolved "ruff" in the radio emission of the classic microquasar SS433 is thought to arise in a disc wind (Blundell et al. 2001).

where

$$x = \frac{r_0 - r_{\min}}{r_{\max} - r_{\min}}. \qquad (2)$$

The parameter $\gamma$ can be used to vary the concentration of poloidal streamlines towards either the inner or outer regions of the wind, but throughout this work we fix it to 1, so the poloidal streamlines are equally spaced in radius.

The poloidal velocity, $v_l$, along a streamline in our model is given by

$$v_l = v_0 + [v_\infty(r_0) - v_0] \frac{(l/R_v)^\alpha}{(l/R_v)^\alpha + 1}, \qquad (3)$$

where $l$ is distance measured along a poloidal streamline. This power-law velocity profile was adopted by SV93 in order to give a continuous variation in the derivative of the velocity and a realistic spread of Doppler-shifted frequencies in the outer portion of the wind ($l > R_v$). We have similar requirements. The initial poloidal velocity of the wind, $v_0$ is (somewhat arbitrarily) set to $6 \, \mathrm{km \, s^{-1}}$ for all streamlines, comparable to the sound speed in the disc photosphere. The wind then speeds up on a characteristic scalelength $R_v$, defined as the position along the poloidal streamline at which the wind reaches half its terminal velocity, $v_\infty$. The terminal poloidal velocity along each streamline is set to a fixed multiple of the escape velocity at the streamline foot point,

$$v_\infty = f v_{\mathrm{esc}}, \qquad (4)$$

so the innermost streamlines reach the highest velocities. The power-law index $\alpha$ controls the shape of the velocity law: as $\alpha$ increases, the acceleration is increasingly concentrated around $l = R_v$ along each streamline. For large $\alpha$, the initial poloidal velocity stays low near the disc and then increases quickly through $R_v$ to values near $v_\infty$.

The wind is assumed to initially share the Keplerian rotation profile of the accretion disc, i.e. $v_{\phi,0}(r_0) = v_K(r_0)$ at the base of the outflow. As the wind rises above the disc and expands, we assume that specific angular momentum is conserved, so that the rotational velocities decline linearly with increasing cylindrical distance from the launch point.

The SV93 prescription also allows us to control the mass loading of the outflow as a function of radius. More specifically, the local mass-loss rate per unit surface area on the disc ($\dot{m}_{\mathrm{wind}}$) is given by

$$\dot{m}_{\mathrm{wind}} \propto \dot{M}_{\mathrm{wind}} r_0^\lambda \cos[\theta(r_0)], \qquad (5)$$

where $\dot{M}_{\mathrm{wind}}$ is the global mass-loss rate through the wind. The run of mass-loss rate per unit area with $r_0$ is illustrated in Fig. 2.

The combination of local mass-loss rate, launching angle and poloidal velocity is sufficient to uniquely determine the density at any point in the wind via a continuity equation (see SV93 for details). The resulting wind is a smooth, single phase outflow without clumps. There is evidence for structure in BALQSO outflows, apparent from complex line shapes (e.g. Ganguly at al. 2006; Simon & Hamann 2010) and time variability (e.g. Capellupo et al. 2011, 2012, 2013), but this is something our simple model cannot address. However, hot star winds and CV winds also exhibit variability and small-scale structure, yet much has been learned about these winds by focusing on the global, underlying smooth flow field. This is the approach followed here.
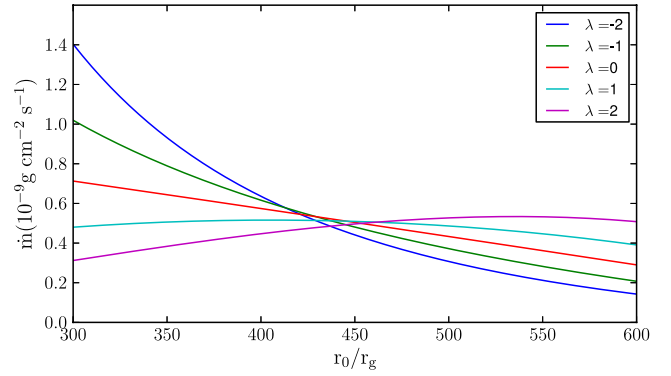


**Figure 2.** Dependence of mass-loss rate per unit area on the disc on radius for three values of $\lambda$. $\dot{M}$ and $\theta(r_0)$ are set as in the benchmark model defined in Section 4.

## 3 IONIZATION, RADIATIVE TRANSFER AND SPECTRAL SYNTHESIS

In order to calculate the spectra predicted to emerge from our disc winds, we use PYTHON, a radiative transfer code designed to model biconical outflows and first described by LK02. The code has been used previously to calculate model spectra for disc-dominated CVs (Noebauer et al. 2010) and young stellar objects (Sim, Drew & Long 2005). Here, we provide a brief overview of the code, focusing particularly on the modifications we have made recently to enable modelling of BALQSOs. All simulations shown in this paper were carried out with version 75 of PYTHON.

### 3.1 Basic structure

PYTHON is a hybrid Monte Carlo/Sobolev radiative transfer code that works by following the progress of energy packets through a simulation grid of arbitrary size, shape and discretization. For the simulations described here, we utilize an azimuthally symmetric cylindrical grid. Energy packets are characterized by a frequency and a weight, defined so that the sum of all packets correctly represents the luminosity and SED of all radiation sources in the model.

The thermal and ionization structure of a wind model is computed iteratively through a series of 'ionization cycles'. During each cycle, energy packets are tracked through the wind and their effect on the wind's temperature and ionization state is computed (see Section 3.3 below). Once the ionization structure of the wind has been determined, a series of 'spectral cycles' are executed, in which synthetic spectra are generated at specific inclination angles.

### 3.2 Radiation sources

For simulations of AGN/QSO, the radiative sources included are a central X-ray source, an accretion disc and the wind itself. We assume that the central source produces a power-law SED and that the optically thick, geometrically thin disc radiates as an ensemble of blackbodies. We do not at present apply the colour temperature correction as suggested in Done et al. (2012) but the correction is in any case modest for the accretion disc in our benchmark model.

The geometry of the X-ray emitting region in AGN is not fully understood, but the emission is believed to arise from a hot corona

above the inner regions of the accretion disc (e.g. Galeev, Rosner & Vaiana 1979). Here, we follow Sim et al. (2008) and assume that the central X-ray source is an isotropically radiating sphere, with radius equal to the innermost radius of the accretion disc [typically set to $r_{ISCO} = 6r_g = 6GM_{BH}/c^2$, the radius of the innermost circular stable orbit (ISCO) for a non-rotating black hole]. The X-ray source produces energy packets governed by a power law in flux, i.e.

$$F_X(\nu) = K\nu^{\alpha_x}, \qquad (6)$$

where $\alpha_x$ is the spectral index. In practice, we characterize the X-ray source primarily by its integrated luminosity between 2 and 10 keV, which is related to $K$ and $\alpha$ via

$$L_X = \int_{2\,keV}^{10\,keV} K\nu^{\alpha_x}\,d\nu. \qquad (7)$$

UV continuum emission in AGN is thought to be dominated by an accretion disc. We assume the disc has the radial temperature profile of the standard thin disc equations (Shakura & Sunyaev 1973), i.e.

$$T_{d,eff}(r_0) = T_\star \left(\frac{r_{BH}}{r_0}\right)^{3/4} \left(1 - \sqrt{\frac{r_{BH}}{r_0}}\right)^{1/4}, \qquad (8)$$

where

$$T_\star = \left(\frac{3\,GM_{BH}\dot{M}_{acc}}{8\sigma\pi r_{BH}^3}\right)^{1/4}. \qquad (9)$$

Here, $\dot{M}_{acc}$ is the accretion rate through the disc, and we take $r_{BH} = r_{ISCO}$, appropriate for a non-rotating SMBH.

Finally, the wind itself is a hot thermal plasma and therefore radiates through various atomic processes including line emission, recombination and/or free–free processes. Unlike the other radiation sources, the radiation field produced by the wind has to be computed iteratively, since it depends on the ionization state and temperature of the outflow. The wind is always assumed to be in radiative equilibrium, i.e. it reprocesses radiation originally produced by the disc and the central source. These components therefore set the total luminosity of the system – the wind is not a *net* source of photons in our model.[2]

## 3.3 Thermal and ionization equilibrium

### 3.3.1 Overall iteration scheme

At the beginning of each simulation, the electron temperature ($T_e$) and ionization state of the wind are initialized by assuming a reasonable value for $T_e$ and adopting LTE ionization fractions. As the energy packets progress through the wind, they lose energy via continuum and line absorption, thereby heating the wind. They can also change frequency in the observer frame via scattering in the outflowing wind. However, since such scattering events are assumed to be coherent in the comoving frame, these frequency changes do not contribute to heating.

As energy packets move through the wind, all of the quantities that are needed to calculate the ionization are logged. These include the frequency-integrated mean (angle-averaged) intensity ($J$), the mean frequency ($\bar{\nu}$) and the standard deviation ($\sigma_\nu$) of the frequency of energy packets passing through the cell. These quantities are

logged in a series of frequency bands to provide information for the ionization calculations described below. We also calculate 'global' values for these quantities (integrated over the entire frequency range) in each cell, for use in the heating and cooling calculations. All energy packets are tracked until they escape the wind.

After each cycle in the ionization stage, a new estimate of $T_e$ is computed via a process of minimizing the absolute value of the difference between $H$, the heating rate computed during the cycle and $C(T_e)$, the cooling rate which is expressed as a function of $T_e$. The code then recomputes the ionization state of the wind, using the new estimate of the temperature and the information recorded about the radiation field in the cell. In order to improve the stability of the code, we restrict the amount by which $T_e$ can change in one ionization cycle.

Armed with new estimates of electron temperature and ionization state, the code then starts the next ionization cycle. This iteration proceeds until the electron temperature in each cell has converged to a stable value. At this point, all physical parameters of the wind are frozen, and synthetic spectra can be produced for any desired wavelength range or inclination angle.

### 3.3.2 Ionization balance

LK02 determined the ionization state of the wind using a 'modified on-the spot approximation' first derived by Abbot & Lucy (1985). This treatment is designed for a situation in which the local radiation field is fairly close to a dilute blackbody, as is the case for O-star winds and CVs. However, unlike O stars and CVs, AGN/QSO emit a significant fraction of their energy in X-rays and have global SEDs that are poorly described by blackbodies.

We have therefore implemented a new method to calculate the ionization state of the wind into PYTHON, which is better suited to situations in which relatively soft (UV) and relatively hard (X-ray) components both contribute significantly to the ionizing radiation field. Our new ionization treatment follows that described by Sim et al. (2008), which can be summarized by the ionization equation

$$\frac{n_{i+1,0}n_e}{n_{i,0}} = \Phi_{T_e}^* \zeta(T_e)S_i(T_e, J_\nu). \qquad (10)$$

Here, $n_e$ is the electron density and $n_{i,0}$ represents the density of the ground state of ionization stage $i$ of a particular atomic species. The quantity $\Phi_{T_e}^*$ is the ratio $n_{i+1,0}n_e/n_{i,0}$ computed via the Saha equation at temperature $T_e$, while $\zeta(T_e)$ is the fraction of recombinations going directly into the ground state, allowing for both radiative recombinations into all levels and dielectronic recombinations. The correction factor $S_i(T_e, J_\nu)$ is the ratio of the photoionization rate expected for the actual SED to that which would be produced by a blackbody at $T_e$,

$$S_i(T_e, J_\nu) = \frac{\int_{\nu_0}^\infty J_\nu \sigma_i(\nu)\nu^{-1}d\nu}{\int_{\nu_0}^\infty B_\nu(T_e)\sigma_i(\nu)\nu^{-1}d\nu}. \qquad (11)$$

Here, $\sigma_i(\nu)$ is the frequency-dependent photoionization cross-section for ionization state $i$, and $J_\nu$ is the monochromatic mean intensity.

This formulation allows us to correctly account for the photoionizing effect of radiation fields with arbitrary SEDs, provided there are sufficient photon packets to adequately characterize the SED. In this work, we model the SED in each cell after each ionization cycle by splitting it into a series of user-defined bands.

---

[2] In principle, it would be simple to allow for non-radiative energy input into the wind (e.g. shocks or energy release via magnetic reconnection events). However, the relevance of these processes, let alone the detailed form they would take, is presently unknown.

Equation (11) can then be re-written as

$$S_i(T_e, J) = \frac{\sum_{\text{band } j=0}^{n} \int_{\nu_j}^{\nu_{j+1}} J_{\nu,j} \sigma_i(\nu) \nu^{-1} \mathrm{d}\nu}{\int_{\nu_0}^{n+1} B_\nu(T_e) \sigma_i(\nu) \nu^{-1} \mathrm{d}\nu}, \tag{12}$$

where the summation in the numerator is now over $n$ bands, each running over a frequency range $\nu_j \to \nu_{j+1}$. In practice, the monochromatic mean intensity in each band is modelled as either a power law,

$$J_{\nu,j} = K_{\text{pl}} \nu^{\alpha_{\text{pl}}}, \tag{13}$$

or an exponential

$$J_{\nu,j} = K_{\text{exp}} e^{(-h\nu/kT_{\text{exp}})}. \tag{14}$$

The values for the four parameters $K_{\text{pl}}$, $\alpha_{\text{pl}}$, $K_{\text{exp}}$ and $T_{\text{exp}}$ are deduced from the two band-limited radiation field estimators mentioned in Section 3.3.1, i.e. $J$ and $\bar{\nu}$. Thus, for each model, the two free parameters are set by requiring that integrating $J_\nu$ and $\nu J_\nu$ over frequency yields the correct values for $J$ and $\bar{\nu}$. The choice between the exponential and power-law models is finally made by comparing the third band-limited estimator of the radiation field, $\sigma_\nu$, to the value predicted by each model.

### 3.3.3 Heating and cooling

Earlier versions of PYTHON accounted for heating and cooling due to free–free, free–bound and bound–bound processes, as well as for adiabatic cooling due to the expansion of the wind. For this study, we have added Compton processes and dielectronic recombinations to the heating and cooling processes included in the code. The former, especially, can be important in QSO winds.

*3.3.3.1 Compton heating and cooling.* Following Sim et al. (2010), we calculate the Compton heating rate in a cell with electron density $n_e$ as

$$H_{\text{comp}} = n_e \sum \bar{f}(\nu) \sigma_C(\nu) W \, \mathrm{d}s, \tag{15}$$

where the summation is carried out over all photon packet paths of length $\mathrm{d}s$ in the cell. Each photon packet carries luminosity (weight) $W$ erg s$^{-1}$ and has frequency $\nu$. Here, $\bar{f}(\nu)$ is the mean energy lost per interaction, equal to $h\nu/m_e c^2$ averaged over scattering angles. The Klein–Nishina formula is used to compute the cross-section $\sigma_C$.

We also include induced Compton heating in our calculations. Following Cloudy & associates (2011), we estimate this heating rate as

$$H_{\text{ind comp}} = n_e \sum \eta_i(\nu) \bar{f}(\nu) \sigma_C(\nu) W \, \mathrm{d}s, \tag{16}$$

where $\eta_i(\nu)$ is the photon occupation number given by

$$\eta_i(\nu) = \frac{J_\nu}{\frac{2h\nu^3}{c^2}}. \tag{17}$$

Finally, the Compton cooling rate ($C_{\text{comp}}$) is given by

$$C_{\text{comp}} = 16\pi V \sigma_T J \frac{kT_e}{m_e c^2}, \tag{18}$$

where $V$ is the volume of the wind cell.

*3.3.3.2 Dielectronic Recombination Cooling.* At the high temperatures expected in a wind irradiated by X-ray photons, dielectronic recombinations can become a significant recombination channel. Even though the associated energy loss from the plasma is never a major cooling process, we include it in our calculations to maintain internal consistency (i.e. processes affecting both ionization and thermal equilibrium should be represented in both calculations). We estimate the cooling rate due to dielectronic recombinations as

$$C_{\text{DR}} = V n_e k T_e \sum_{\text{All ions}} n_i \alpha_{\text{DR}}^i(T_e), \tag{19}$$

where $\alpha_{\text{DR}}^i(T_e)$ is the temperature-dependent dielectronic recombination rate coefficient for each ion in a cell. The main approximation made in this equation is that the energy removed from the electron pool per dielectronic recombination is equal to the mean kinetic energy of an electron ($\simeq kT_e$).

### 3.3.4 Code validation

In order to validate the design and implementation of our ionization algorithm, we have carried out a series of tests against the well-known photoionization code CLOUDY (Ferland et al. 2013). In these tests, we consider a geometrically thin spherical shell illuminated by a wide range of input SEDs, including specifically SEDs with significant X-ray power-law components. We generally find good agreement between the ionization states predicted by PYTHON and CLOUDY in these tests for species important in the BAL context. We also find good agreement in the predicted electron temperatures for quite a wide range of models.

One example of these tests is shown in Fig. 3. Here, we plot the relative abundances of the various ionization stages of carbon as a function of ionization parameter

$$U = \frac{Q_{\text{H}}}{4\pi R^2 n_{\text{H}} c} \tag{20}$$

$$= \frac{\int_{13.6\text{eV}}^{\infty} (L_\nu/h\nu) \mathrm{d}\nu}{4\pi R^2 n_{\text{H}} c} \tag{21}$$

$$= \frac{4\pi}{n_{\text{H}} c} \int_{13.6\text{eV}}^{\infty} \frac{J_\nu \mathrm{d}\nu}{h\nu}, \tag{22}$$
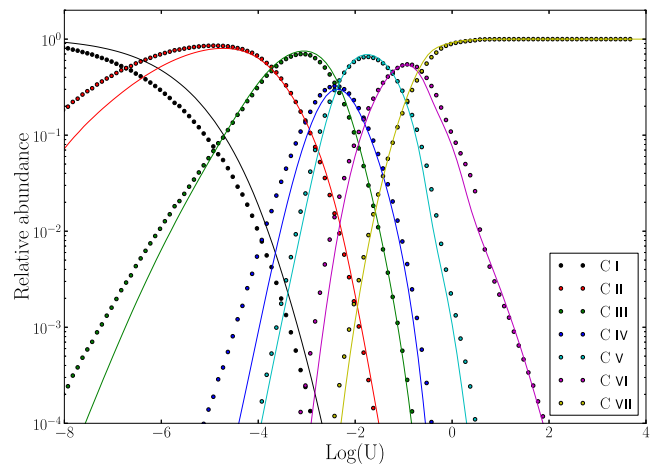


**Figure 3.** Relative abundance of different carbon ionization stages for a range of ionization parameters $U$. Calculations carried out in a thin shell geometry illuminated by a broken power law. Symbols are predictions from PYTHON and lines are predictions from CLOUDY.

where $Q_H$ is the number of hydrogen-ionizing photons emitted by the illuminating source per second, $R$ is the distance to the source, $n_H$ is the local hydrogen number density and $c$ is the speed of light. $L_\nu$ is the monochromatic luminosity. The ionization parameter is a measure of the ratio of the ionizing photon density and the local matter density. As such, it is a good predictor of the ionization state of optically thin photoionized plasmas.

In the test shown in Fig. 3, the irradiating SED was modelled as a doubly broken power law with $\alpha = 2.5$ below 0.136 eV, $\alpha = -2$ above 20 keV and $\alpha = -0.9$ between these break frequencies. This was in order to allow direct comparison with a CLOUDY model defined via the power-law command. The spherical shell was assumed to lie at $R = 10^{11}$ cm, the hydrogen density was taken to be $n_H = 10^7$ cm$^{-3}$ and the ionization parameter was adjusted by varying the luminosity of the ionizing SED. With such a simple set-up, both the SED and the geometry can be modelled in exactly the same way in both PYTHON and CLOUDY. Given the likely differences in detailed atomic physics and atomic data used in CLOUDY and PYTHON, there is good agreement between the codes, especially for the moderately to highly ionized stages of carbon that we expect to see in the vicinity of a QSO.

As noted above, the electron temperatures predicted by PYTHON and CLOUDY also generally agree quite well. One exception to this is situations in which iron lines dominate the cooling, where PYTHON can overestimate the temperature by as much as a factor of about 2. Some wind regions in our benchmark model are likely to be affected by this. However, since the electron temperature only appears in the ionization equation via $\sqrt{T_e}$, the effect of this issue on the relevant ionization fractions in our models is relatively small.

### 3.4 Spectral synthesis

Once the thermal and ionization state of the wind has converged, the ionization cycles are terminated and the spectral cycles begin. In the latter, the thermal and ionization structure are considered fixed, and photons are only generated over the restricted frequency range for which detailed predictions are needed. This saves CPU time and allows us to achieve much greater spectral resolution and signal-to-noise in the simulated spectra.

The spectra themselves are extracted from the Monte Carlo simulation using the techniques described by LK02. Collisionally excited line emission is treated in the two-level atom approximation, which is acceptable for strong resonance lines in which the upper level is populated by transitions from the lower (ground) state. Most of the transitions associated with BALs and BELs fall into this category. However, this approximation is *not* adequate for many other transitions, most notably the Hydrogen Lyman and Balmer series, for which the upper states are populated by a radiative recombination cascade. Sim et al. (2005) have already used a more general method to model infrared H I line emission in YSOs with PYTHON; work is in progress on implementing this treatment into our simulations of AGN/QSOs.

### 3.5 Atomic data

For the calculations described in this paper, we include atomic data for H, He, C, N, O, Ne, Na, Mg, Al, Si, S, Ar, Ca and Fe. Elemental abundances are taken from Verner, Barthel & Tytler (1994) and the basic atomic data, such as ionization potential and ground-state multiplicities, are taken from Verner, Verner & Ferland (1996). For H, He, C, N, O and Fe, we use TOPBASE (Cunto et al. 1993) data for energy levels and photoionization cross-sections from both ground-state and excited levels. For other elements, we use the analytic approximations for ground-state photoionization cross-sections given

in Verner et al. (1996). For bound–bound transitions, we use the line list given in Verner et al. (1996), which contains nearly 6000 ground-state-connected lines. The levels associated with these lines are computed from the line list information using a method similar to that described by Lucy (1999).

We adopt dielectronic recombination rate coefficients and total radiative rate coefficients from the CHIANTI data base version 7.0 (Dere et al. 1997; Landi et al. 2012). Ground-state recombination rates are taken from Badnell (2006) where available and otherwise computed from the photoionization data via the Milne relation. Finally, we use Gaunt factors for free–free interactions given by Sutherland (1998).

## 4 A BENCHMARK DISC WIND MODEL FOR BALQSOs

One of the main challenges in trying to model BALQSOs is that the physical characteristics of the disc winds that produce the BALs are highly uncertain. The kinematic model described in Section 2 is sufficiently flexible to describe a wide range of outflow conditions, but the price for this flexibility is a potentially huge parameter space. We have therefore used a variety of theoretical and observational constraints (and considerable trial and error) to design a benchmark disc wind model whose predicted spectrum resembles that of a BALQSO (for sightlines cutting through the outflow).

Since we have not yet carried out a systematic exploration of the relevant parameter space, we make no claim that this fiducial model is optimal, nor that it faithfully describes reality. Indeed, in Section 6, we will discuss some of its shortcomings. However, we believe it is nevertheless extremely useful as a benchmark. More specifically, it provides (i) a first indication of what can be realistically expected of disc wind models; (ii) a better understanding of the challenges such models face; (iii) a convenient starting point for further explorations of parameter space.

In the rest of this section, we will discuss the constraints that have informed our choice of parameters for the benchmark model, which are summarized in Table 1.

### 4.1 Basic requirements: BALnicity and ionization state

Our primary aim here is to find a set of plausible parameters for a QSO wind that yield synthetic spectra containing the features expected of a BALQSO from a range of viewing angles. As noted in Section 1, in the majority of BALs, the HiBALs, the absorption features are due to highly ionized species such as N V $\lambda\lambda$1240, C IV $\lambda\lambda$1550 and Si IV $\lambda\lambda$1400. The C IV feature, in particular, is most often used to identify BALQSOs, so we judge the initial success of candidate wind models by their ability to produce this feature. In practice, this is primarily a constraint on the ionization state of the wind: we require that C IV should be present – if not necessarily dominant – throughout an appreciable fraction of the outflow.

BALs are usually identified via the so-called BALnicity index (BI) (Weyman et al. 1991), which is a measure of absorption strength in the velocity range between $-3000$ and $-25000$ km s$^{-1}$. It is therefore not sufficient to produce C IV anywhere in the outflow – in order for the model to resemble a BAL, C IV needs to be present in reasonable concentrations in regions characterized by the correct velocities.

### 4.2 Black hole mass, accretion rate and luminosity

Our goal is to model a fairly typical, high-luminosity (BAL)QSO, so we adopt a black hole mass of $10^9$ M$_\odot$, along with an Eddington

**Table 1.** Wind geometry parameters used in the benchmark model.

| Free parameters | Value |
|---|---|
| $M_{BH}$ | $1 \times 10^9 \, M_\odot$ |
| $\dot{M}_{acc}$ | $5 \, M_\odot \, yr^{-1} \simeq 0.2 \, \dot{M}_{Edd}$ |
| $\alpha_X$ | $-0.9$ |
| $L_X$ | $1 \times 10^{43} \, ergs \, s^{-1}$ |
| $r_{disc}(min) = r_X$ | $6r_g = 8.8 \times 10^{14} \, cm$ |
| $r_{disc}(max)$ | $3400r_g = 5 \times 10^{17} \, cm$ |
| $\dot{M}_{wind}$ | $5 \, M_\odot \, yr^{-1}$ |
| $r_{min}$ | $300r_g = 4.4 \times 10^{16} \, cm$ |
| $r_{max}$ | $600r_g = 8.8 \times 10^{16} \, cm$ |
| $\theta_{min}$ | $70\overset{\circ}{.}0$ |
| $\theta_{max}$ | $82\overset{\circ}{.}0$ |
| $\lambda$ | $0$ |
| $v_\infty$ | $v_{esc}(f{=}1)$ |
| $R_v$ | $1 \times 10^{18} \, cm$ |
| $\alpha$ | $1.0$ |
| Derived parameters | Value |
| $L_\nu(2500 \, \text{Å})$ | $6.3 \times 10^{30} \, erg \, s^{-1} \, Hz^{-1}$ |
| $L_\nu(2 \, keV)$ | $1.2 \times 10^{25} \, erg \, s^{-1} \, Hz^{-1}$ |
| $L_{bol}$ | $2.4 \times 10^{46} \, erg \, s^{-1}$ |
| $M_{bol}$ | $-27.4$ |
| $M_u$ | $-26.2$ |
| $\alpha_{ox}$ | $-2.2$ |

ratio of $\epsilon = 0.2$. For an assumed accretion efficiency of $\eta = 0.1$, this corresponds to an accretion rate of $\dot{M}_{accretion} \sim 5 \, M_\odot yr^{-1}$ and a bolometric disc luminosity of $L_{bol} \simeq 2.4 \times 10^{46} \, erg \, s^{-1}$.

### 4.3 Outflow geometry

BALQSOs represent $\simeq 20$ per cent of all QSOs (e.g. Hewett & Foltz 2003; Knigge et al. 2008, but also see Allen et al. 2011). There are two obvious ways to interpret this number: (i) either all QSOs spend $\simeq 20$ per cent of their life as BALQSOs ('evolutionary unification'; e.g. Becker et al. 2000), or (ii) all QSOs contain disc winds, but the resulting BAL signatures are visible only from $\simeq 20$ per cent of all possible observer orientations ('geometric unification'; e.g. Elvis 2000).[3] Here, we adopt the geometric unification picture, with the aim of testing its viability.

As illustrated in Fig. 4, our wind geometry allows for three distinct classes of sightline towards the central engine. Looking from the polar direction, 'above the wind cone', the sightline does not intersect the wind at all, and looking from the equatorial direction, the sightline passes through the base of the wind cone where the projected line-of-sight velocities are too low to produce BAL features. We anticipate that BAL features will result when the central engine (or, strictly speaking, the UV bright portions of the accretion disc) are viewed from the third class of sightline – looking 'into the wind cone'. We therefore expect such sightlines to subtend $\simeq 20$ per cent of the sky as seen by the central engine. Note that this description of the sightlines only applies to models like our benchmark model, in which most of the emission arises from inside the wind launching radius.

---

[3] This could be an underestimate, since intrinsic BALQSO fractions tend to be derived from magnitude-limited samples, with no allowance for the possibility that foreshortening, limb-darkening or wind attenuation may reduce the continuum flux of a typical BALQSO relative to that of a typical QSO (Krolik & Voit 1998). For the purpose of this paper, we ignore this potential complication.
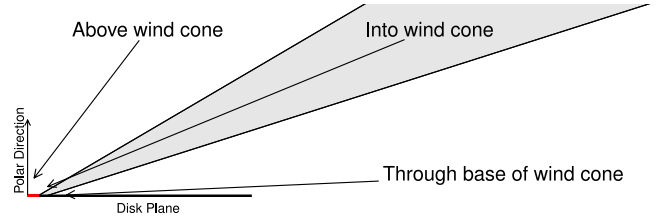


**Figure 4.** Cartoon illustrating the three broad classes of sightline discussed in the text.

If we define $\theta_{min}$ and $\theta_{max}$ as the angles made by the inner and outer boundaries of the wind with respect to the disc normal, these constraints translate into a simple relationship between $\theta_{min}$ and $\theta_{max}$, i.e.

$$0.2 = \cos(\theta_{min}) - \cos(\theta_{max}). \tag{23}$$

Most geometrical unification scenarios assume that BAL-producing QSO winds flow predominantly along the equatorial plane of the disc, rather than along the polar axis (e.g. Weyman et al. 1991; Ogle et al. 1999; Elvis 2000; however, see Brotherton, De Breuck & Schaefer 2006; Zhou et al. 2006 for a contrary view). In line with this general view, we have found that ionization states capable of producing C IV and other typical BAL features are more naturally produced in equatorial, rather than polar disc winds. This is because one of the main challenges faced by disc wind models is to prevent the over-ionization of the outflow by the central X-ray source (see below). Other things being equal, equatorial winds are less ionized, partly because of limb darkening, and partly because the disc appears foreshortened from equatorial directions. In addition, in geometries like ours, where the wind arises from parts of the disc radially outside the location where the ionizing radiation is produced, an equatorial wind exhibits self-shielding, i.e. the radiation must pass through the inner parts of the wind to reach the outer parts. Therefore, the ionization state can be lower than for a polar wind, where all parts of the wind can see the ionizing radiation directly.

Based on these considerations, we adopt a mostly equatorial geometry with $\theta_{min} = 70°$ and $\theta_{max} = 82°$ for our benchmark model. With this choice, 66 per cent of the remaining sightlines lie 'above' the wind cone, while 14 per cent view the central source through the base of the wind. If geometric unification is correct and complete – in the sense that the emission lines in non-BAL QSOs are produced by the same outflow that produces the absorption features seen in BALQSOs (e.g. Elvis 2000) – we would ideally see different classes of QSO as we view a given system from the three distinct types of viewing angles.

### 4.4 Wind-launching region

There is no consensus on the location of the wind-launching region on the accretion disc. However, there are several empirical and theoretical considerations that can inform the design of our benchmark model.

First, within the geometric unification scenario, QSO disc winds are responsible not only for BAL features, but also for the broad emission lines (BELs) seen in non-BAL QSOs. We can therefore use the result of reverberation mapping studies of this broad line region (BLR) to guide us in locating the outflow. Kaspi et al. (2000) have carried out reverberation mapping of the C IV BLR for high-luminosity quasars. A representative example is S5 0836+71, a quasar with a black hole mass of $2.6 \times 10^9 \, M_\odot$, for which they

found a rest-frame delay of 188 d. This implies a distance of the line-forming region from the UV continuum source of $1260 \, r_{\rm g}$.[4] Since the C IV line-forming region may lie substantially downstream in the outflow, this is an upper limit on the distance of the launching region from the centre.

Secondly, BAL features exhibit variability on time-scales from days to years (e.g. Capellupo et al. 2011, 2012, 2013). If interpreted in terms of wind features crossing our line of sight, the *shortest* variability time-scales – which arise in the innermost parts of the line-forming region – correspond to distances of $\sim 3 \times 10^{16}$ cm or, equivalently, $\sim 200 \, r_{\rm g}$ from the centre (for an assumed $M_{\rm BH} \simeq 10^9 \, {\rm M}_\odot$).

Thirdly, one of the most promising mechanisms for driving QSO disc winds is via radiation pressure in spectral lines (e.g. Proga, Stone & Kallman 2000; Proga & Kallman 2004). Empirical support for this idea comes from the presence of the 'ghost of Lyman $\alpha$' in some N V BAL features (see Arav et al. 1995; Arav 1996; North, Knigge & Goad 2006; but also see Cottis et al. 2010). In published simulations where such winds are modelled in a physically consistent manner, the typical launching radii are (a few) $\times 100 \, r_{\rm g}$ (e.g. Proga et al. 2000; Risaliti & Elvis 2010).

Fourthly and finally, it is physically reasonable to assume that the maximum velocity achieved by the outflow corresponds roughly to the fastest escape velocity in the wind-launching region on the accretion disc. Observationally, $v_{\rm max} \sim 20\,000 \, {\rm km \, s^{-1}}$, which, for a $10^9 \, {\rm M}_\odot$ black hole, corresponds to the escape velocity from $\simeq 400 \, r_{\rm g}$.

Taken together, all of these considerations suggest that a reasonable first guess at the location of the wind-launching region on the disc is of the order of a few hundred $r_{\rm g}$. In our benchmark model, we therefore adopt $r_{\rm min} = 300 \, r_{\rm g}$ and $r_{\rm max} = 600 \, r_{\rm g}$.

## 4.5 Wind mass-loss rate

One of the most fundamental parameters of any wind model is the mass-loss rate into the outflow, $\dot{M}_{\rm wind}$. In our benchmark model, we set $\dot{M}_{\rm wind} = \dot{M}_{\rm acc} = 5 \, {\rm M}_\odot \, {\rm yr}^{-1}$. This value was arrived at mainly by trial and error, but with a conservative preference for values satisfying $\dot{M}_{\rm wind} \lesssim \dot{M}_{\rm acc}$. As shown explicitly in Section 6.1, in practice, we found that we required $\dot{M}_{\rm wind} \simeq \dot{M}_{\rm acc}$ in order to produce BAL features for even modest X-ray luminosities.

Strictly speaking, any model with $\dot{M}_{\rm wind} \gtrsim \dot{M}_{\rm acc}$ is not entirely self-consistent, since the presence of such an outflow would alter the disc's temperature structure (e.g. Knigge 1999). However, we neglect this complication, since the vast majority of the disc luminosity arises from well within our assumed wind-launching radius. Thus, even though our model ignores that the accretion rate *is* higher further out in the disc, it correctly describes the innermost disc regions that produce virtually all of the luminosity.

Finally, in the absence of evidence to the contrary, we take the simplest possible prescription for the run of the mass-loss rate with radius across the wind-launching region, i.e. $\lambda = 0$ (see equation 5 in Section 2).

## 4.6 Velocity law parameters

Ideally, the parameters defining the poloidal velocity law of the wind would be predicted by the relevant acceleration mechanism.

However, since this is not yet possible, we have simply adopted parameters that result in reasonably BAL-like C IV features.

As noted in Section 4.4 above, it seems physically plausible that the terminal outflow velocity along a poloidal streamline will roughly reflect the local escape velocity at the streamline footpoint. Having already adopted wind launching radii based on this idea, we therefore also adopt $v_\infty = v_{\rm esc}$, i.e. $f = 1$ in equation (4).

The other two parameters defining the poloidal velocity law are $R_v$, the poloidal distance at which the velocity is equal to half the terminal velocity, and $\alpha$, the exponent describing how the velocity varies with poloidal distance. As discussed above, the locations of BAL- and BEL-forming regions within the wind likely extend to distances of up to about $2000 \, r_{\rm g}$, so this is a reasonable number to adopt for $R_v$. For the $10^9 \, {\rm M}_\odot$ black hole in our benchmark model, this corresponds to $R_v = 10^{18}$ cm. Finally, in the absence of other information, we adopt $\alpha = 1$. This produces a relatively slow acceleration as a function of poloidal distance along a streamline and seems to produce reasonable BAL shapes. We will explore the effect of changing these parameters in future work.

## 4.7 X-ray spectrum and luminosity

The X-ray luminosity of the central source is set to $L_X = 10^{43} \, {\rm erg \, s^{-1}}$ in our benchmark model. This value was arrived at through the requirement that the model should produce BALs which constrains the X-ray luminosity, since X-rays can strongly affect the ionization state of the outflow. We set the spectral index of the X-ray spectrum to $\alpha_X = -0.9$, as suggested by Giustini, Cappi & Vignali (2008).

Quasar spectra are often characterized in terms of the ratio of X-ray to bolometric (or UV) luminosity. This ratio is usually characterized by the spectral index between X-rays and optical/UV, $\alpha_{\rm ox}$, defined as

$$\alpha_{\rm ox} = 0.3838 \log \left( \frac{L_\nu(2 \, keV)}{L_\nu(2500 \, \text{\AA})} \right), \tag{24}$$

where $L_\nu(2 \, {\rm keV})$ and $L_\nu(2500 \, \text{\AA})$ are the inferred monochromatic luminosities at $2 \, {\rm keV}$ (X-ray) and $2500 \, \text{\AA}$ (UV), respectively. Ignoring the angle dependence of the disc emission, we obtain a mean value of $\alpha_{\rm ox} \sim -2.2$ for the parameters used in our benchmark model. This is considerably lower than observed in typical non-BAL QSOs (Just et al. 2007) and lies near the lower (X-ray weak) end of the range of $\alpha_{\rm ox}$ seen in BALQSOs (e.g. Giustini et al. 2008; Gibson et al. 2009). The X-ray weakness of the model, as well as the sensitivity of our results to the adopted X-ray luminosity, are discussed in more detail in Section 6.1.

## 4.8 Size and resolution of the numerical grid

The outer edge of our simulation grid is set to $1 \times 10^{19}$ cm. This is large enough to ensure that all spectral features of interest arise entirely within the computational domain. In all simulations shown in this paper, this domain is sampled by a cylindrical grid composed of $100 \times 100$ logarithmically spaced cells. We have carried out resolution tests to ensure that this is sufficient to resolve the spatially varying physical conditions and ionization state of the outflow.

## 5 RESULTS AND ANALYSIS

Having defined a benchmark disc wind model for AGN/QSOs, we are ready to examine its predicted physical and observable characteristics. In Section 5.2, we will present synthetic spectra

---

[4] Note that the UV continuum is produced at very small radii compared to the wind launch radius and so can be treated as originating from the centre of the model for these estimates
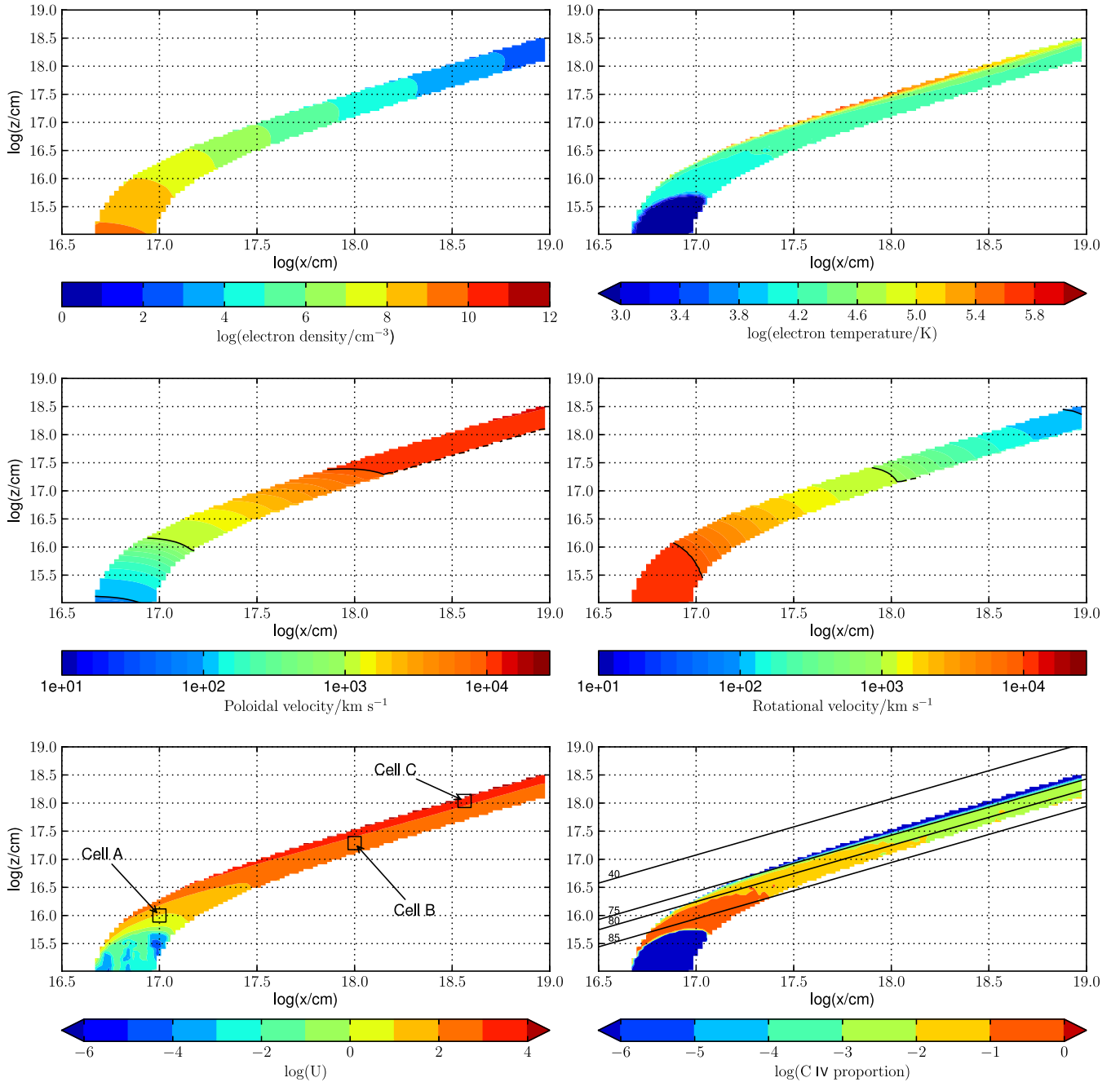
**Figure 5.** The electron density (top left), electron temperature (top right), poloidal velocity (middle left), rotational velocity (middle right), ionization parameter (bottom left) and proportion of C ions in the C IV ionization state (bottom right) for the benchmark model. Only the positive *x–z* plane is shown, the wind is rotationally symmetrical around the *z* axis. Note the logarithmic scales and the difference in scales for the *x* and *z* axes. The location of cells for which 'cell' spectra are presented in Fig. 6 are shown in the ionization parameter plot and the black lines on the C IV plot show sightlines through the wind to the origin used to produce the spectra plotted in Fig. 7.

reminiscent of BALQSOs for sightlines looking into the wind cone. However, it is helpful to examine the physical and ionization state of the benchmark model before analysing these spectra in detail.

### 5.1 The physical state of the outflow

The top four panels in Fig. 5 show a selection of physical parameters of the converged wind model. Considering first the electron density (top-left panel), we see that our choice of kinematic parameters has given rise to an outflow with a fairly high density of $n_{\rm H} \sim 10^{10}\,{\rm cm}^{-3}$

at its base. However, this declines quickly as we move outwards, due to the expansion and acceleration of the wind. Hydrogen is fully ionized throughout the entire outflow, so $n_{\rm H} \simeq n_e$ everywhere.

The electron temperature in the wind ranges from $\sim 10^3\,K$ near the base of the wind to more than $10^5\,K$ (top-right panel). The highest temperatures are in a thin layer near the 'top' of the wind, at distance of $\simeq 10^{18}\,{\rm cm}$ from the central engine. These regions are hot because they are directly exposed to the radiation field of the accretion disc and the X-ray source. These regions also shield the wind material 'behind' them, however, and thus help to ensure
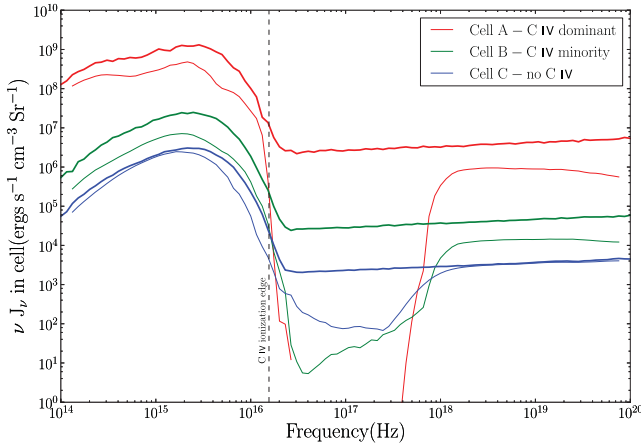
**Figure 6.** Mean specific intensity in three cells. The solid line (red in the online version) is a cell with C IV as the dominant Carbon ionization stage, in the base of the wind. The dashed line (green in the online version) is for a cell with significant C IV in a fast moving part of the wind, and the dotted line (blue in the online version) is for a cell at the top of the wind, fully exposed to the ionizing continuum. The thick lines represent the unobscured spectrum that would be seen in that region. The vertical line marks the location of the C IV photoionization edge.

more moderate temperatures in the rest of the outflow. In fact, much of the disc wind is heated to temperatures near $T_e \sim 10^4$ K, which are quite conducive to the formation of the high-ionization lines typically seen in (BAL)QSOs, such as C IV, Si IV and N V.

The middle panels of Fig. 5 illustrate the velocity structure of our benchmark model, separated into poloidal (middle-left panel) and rotational (middle-right panel) components. The poloidal velocities show the relatively gradual speed-up of the outflow as a function of distance, which is due to our choice of velocity law exponent. As one would expect, low velocities are found near the base of the wind and high velocities are reached only quite far out. It is this variation in poloidal velocity which produces BAL features as photons produced by the effectively point-like central UV source are scattered out of the line of sight by progressively faster moving wind parcels.

By contrast, the highest rotational velocities are found near the disc plane, where they are effectively equal to the Keplerian velocities in the disc. They then decline linearly with increasing cylindrical distance from the rotation axis, because we assume that wind material conserves specific angular momentum. The projected rotational velocity along a sightline to the central source is zero (or nearly so), and therefore rotational velocities do not play a major part in the formation of BAL features, although they should help in producing BELs.

The bottom-left and right-hand panels in Fig. 5 show the ionization parameter and C IV ionization fraction throughout the outflow, respectively. Interestingly, the model generates sufficient concentrations C IV to make strong BALs even though $U > 1$ throughout most of the wind. This contrast with the results shown for a thin-shell model in Fig. 3, where this ion is not present for such values of $U$. The main reason for this difference is that the wind is self-shielding: absorption in the inner parts of the outflow (primarily due to photoionization) can strongly modify the SED seen by the outer parts of the wind. This, in turn, changes the ionization parameter at which particular ions are preferentially formed. Fig. 6 illustrates the effect of the self-shielding on the SED seen by different parts of the outflow.

## 5.2 Observing the model: synthetic spectra

Fig. 7 shows the spectra we predict for observers located along the directions indicated in the lower-right panel of Fig. 5. These viewing angles correspond to sightlines to the central source that look above the wind cone ($i = 40°$), into the wind cone ($i = 75°$ and $i = 80°$), and through the base of the wind cone ($i = 85°$). For comparison, we also show a pure, unobscured continuum spectrum for each viewing angle; these continua were generated by re-running the model with the wind density set to a negligible value.

### 5.2.1 Sightlines looking into the wind cone

The two middle panels in Fig. 7 show the emergent spectra for sightlines through the wind ($i = 75°$ and $i = 80°$). These spectra clearly contain BALs, i.e. broad, blue-shifted absorption features associated with several strong, high-ionization lines in the UV region. More formally, we calculate BIs of $11\,400\,\mathrm{km\,s^{-1}}$ ($i = 75°$) and $9900\,\mathrm{km\,s^{-1}}$ ($i = 80°$) for the C IV lines we predict for these two sightlines. Thus, observed systems displaying these spectra would certainly be classified as bona-fide BALQSOs. This is one of the main results of our work.

Many of the transitions exhibiting BAL features in the spectra for both sightlines also show a redshifted emission component, forming the other part of the classic P-Cygni profile seen in such sources. This can be interpreted as the red-shifted part of a classic rotationally broadened, double-peaked emission line, which is produced primarily by scattering in the base of the wind. The blue-shifted part of the line profile is not visible, since it is superposed on and/or absorbed by the BAL feature.

Another interesting feature of the BAL spectra is that the Si IV absorption feature is narrower than the C IV feature for all sightlines. This is due to the lower ionization potential of the silicon ion, meaning that it is produced in a more limited part of the wind. The relative strengths of features is broadly in agreement with observations (Gibson et al. 2009) and demonstrates that, at least to first order, we are predicting the correct ionization state in the BAL-forming portion of the wind.

The continuum for both sightlines through the wind is suppressed relative to the unobscured SED (see Fig. 7). This attenuation of the continuum is predominantly due to electron scattering. The optical depth to electron scattering through the wind is shown in Fig. 8, along with the corresponding attenuation factor, $F/F_0 = e^{-\tau_{es}}$. For example, at $i = 75°$ our model gives $\tau_{es} \simeq 0.3$ and $F/F_0 \simeq 0.7$, in agreement with Fig. 7.

Detailed C IV line profiles predicted by our model for a more finely spaced grid of sightlines are shown in Fig. 9, along with the BI calculated for each profile. BALs (i.e. features with BI > 0) are observed for inclinations $73° < i < 83°$, which represents $\simeq 17$ per cent of all possible sightlines.

### 5.2.2 Sightlines looking above the wind cone

We now consider the $i = 40°$ sightline, which views the central engine from 'above' the wind cone. In a pure geometric unification scenario, this sightline may be expected to produce a classic Type I QSO spectrum. What we observe from the simulation is a slightly enhanced continuum, along with some broad, but weak emission lines (as in Sim et al. 2008).

The continuum enhancement is mainly due to electron scattering *into* this line of sight. As we have seen in Section 5.2.1 and Fig. 8, the base of the wind is marginally optically thick to electron scattering
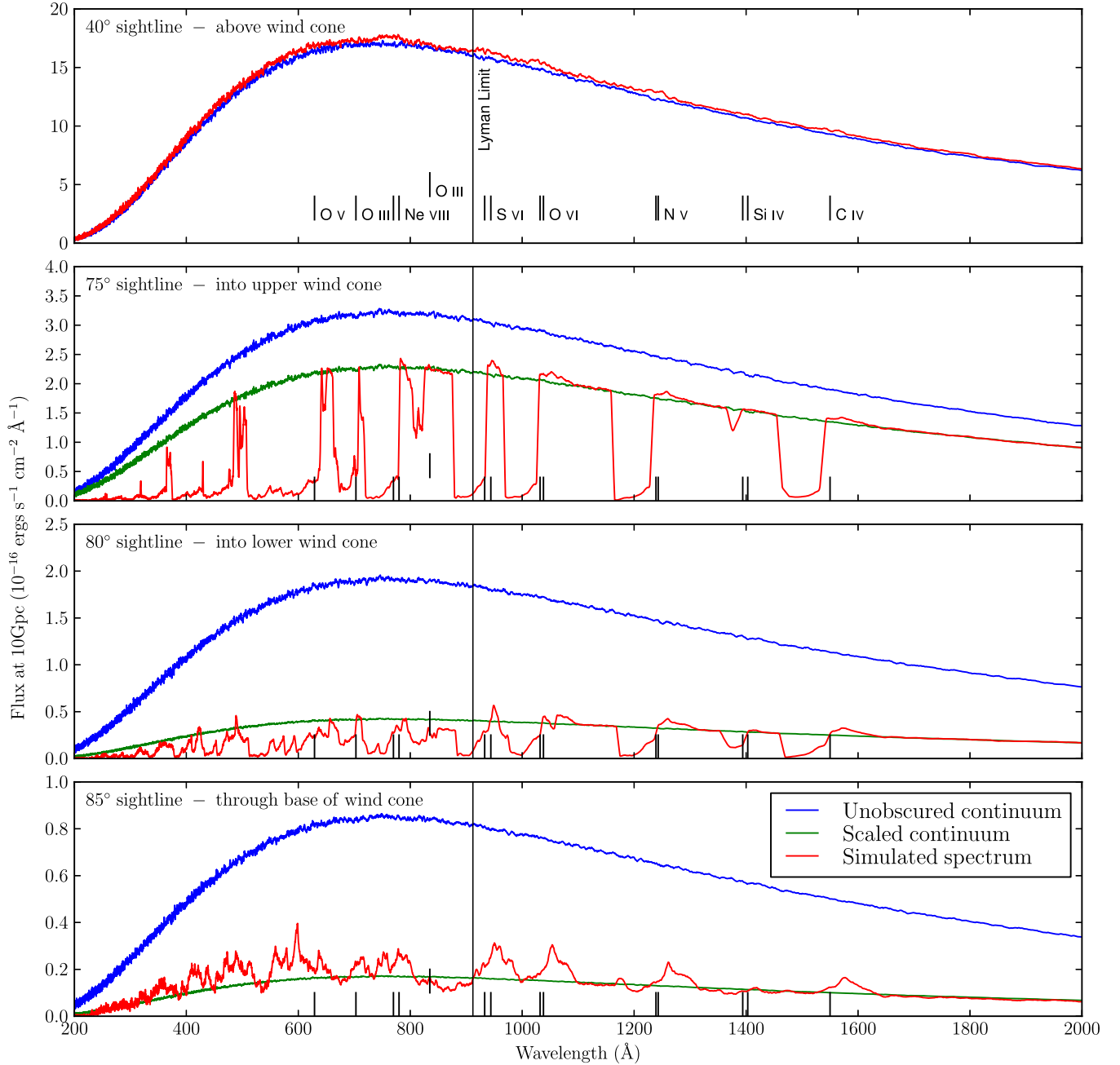
**Figure 7.** Simulated spectra for four sightlines. The top panel shows the 40° sightline, over the top of the wind to the brightest parts of the accretion disc, whilst the next panel shows the 75° sightline, looking through the upper parts of the wind. The next panel is for 80° looking through the lower part of the wind and finally, the bottom panel shows the 85° sightline which is almost equatorial, and views the bright central source through the very base of the wind. For each sightline, the unobscured continuum is also plotted for comparison along with a scaled continuum. The scaled continuum is the unobscured continuum scaled to equal the simulated spectrum away from line features, and therefore takes account of electron scattering. The location of some of the spectral features most relevant for BALQSOs are marked.

in directions along the disc plane. Thus, photons scattering in this region tend to emerge preferentially along the more transparent sightlines perpendicular to this plane, and the wind essentially acts as a reflector.

More importantly, the emission lines superposed on the continuum do correspond to the typical transitions seen in Type I QSOs, but they are weaker than the observed features. For example, the C IV emission line in our model has an equivalent width of only 1.4 Å. By contrast, the equivalent with of the C IV line in a typical QSO with a continuum luminosity of $L_\lambda(1550\,\text{Å}) \simeq 10^{43}$ erg s$^{-1}$

is $\simeq 60$ Å (Xu et al. 2008). Other sightlines above the wind cone ($0° \leq i \leq 70°$) yield qualitatively similar spectra. Overall, the presence of the right 'sort' of emission lines is encouraging, but their weakness is an obvious shortcoming of the model. We will discuss the topic of line emission in more detail in Section 6.2.

### 5.2.3 Sightlines looking through the base of the wind cone

Let us finally consider the highest inclinations, which correspond to sightlines that do not lie along the wind cone, but for which the
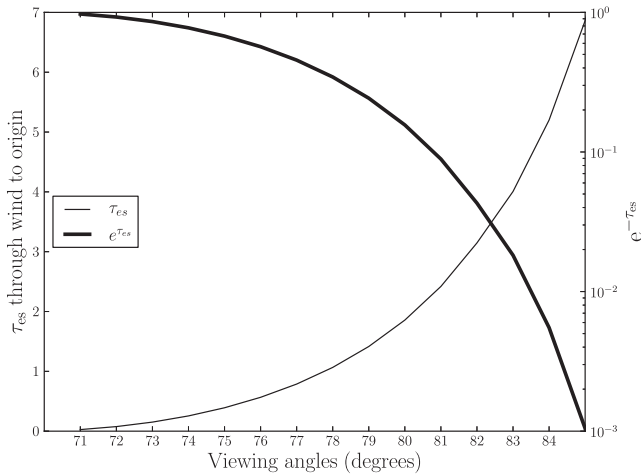
**Figure 8.** Electron scattering optical depth through the wind towards the origin. The heavy line is the expected attenuation.

UV continuum source (i.e. the central region of the accretion disc) is viewed through the dense, low-velocity base of the outflow. It is not obvious what type of QSO one might expect to see from such sightlines, since in the standard model of QSOs, one might expect the torus to obscure such sightlines.

Fig. 8 shows that the $\tau_{es} > 7$ for this inclination, and indeed we find that essentially all of the radiation emerging from the model in this direction has been scattered several times within the wind before ultimately escaping along this vector. This is in line with results presented by Sim et al. (2010), who found that, for Compton-thick winds, AGN spectra at high inclination are dominated by scattered radiation. Recent observational work (e.g. Treister, Urry & Virani 2009) has demonstrated that there is a population of AGN in the local Universe where the X-ray source is completely obscured, and the X-ray spectrum is dominated by reflection. These high-inclination sightlines could represent these so-called 'reflection-dominated Compton-thick AGN'.

The shape of the predicted emission features is dominated by the rotational velocity field in the wind. Taking C IV as an example and examining Fig. 5, we see that the fractional abundance peaks in a region where the rotational velocity is significantly higher than the outflow velocity. Scattering from this region (along with any thermal emission) will produce the double-peaked line profile that is characteristic of line formation in rotating media (e.g. Smak 1981; Marsh & Horne 1988). The blue part of this profile is then likely suppressed, since it is superposed on and/or absorbed by blue-shifted absorption in the base of the wind.

# 6 DISCUSSION

The results shown in the previous section confirm that a simple disc wind model can produce the characteristic BAL features seen in about $\simeq 20$ per cent of QSOs. However, they also reveal some significant shortcomings of the model. In this section, we will consider some of the key questions raised by our results in more detail and point out promising directions for future work.

## 6.1 The sensitivity of BAL features to X-ray luminosity

As noted in Section 4.7, our benchmark model is rather X-ray weak compared to most real (BAL)QSOs. To quantify this, Fig. 10 shows the viewing angle dependence of $\alpha_{ox}$ for our benchmark model.

Clearly, $\alpha_{ox}$ (i.e. the X-ray to optical ratio) is a strong function of inclination. Two effects are responsible for this.

First, the UV and optical fluxes are dominated by the accretion disc and thus decline steeply with inclination, due to foreshortening and limb darkening. By contrast, the X-ray source is assumed to emit isotropically (although the disc can obscure the 'lower' hemisphere). Thus, in the absence of any outflow, $\alpha_{ox}$ increases with inclination, as the X-rays become relatively more important. This is the trend marked by the solid line in Fig. 10.

Secondly, sightlines to the central engine that cross the wind cone can be affected by absorption and radiative transfer in the outflow. In particular, bound-free absorption preferentially suppresses the X-ray flux along such sightlines in our model, and hence reduces $\alpha_{ox}$. The crosses in Fig. 10 show the predicted values of $\alpha_{ox}$ taking both effects into account. This shows that the suppression of $\alpha_{ox}$ is strongest for sightlines looking directly into the wind, i.e. the same viewing angles that produce BALs.

For our benchmark model, we find that $\alpha_{ox} = -2.44$ for $i = 40°$ and $\alpha_{ox} = -2.89$ for $i = 75°$. If these viewing angles can be taken to represent non-BAL QSOs and BALQSOs, respectively, we can compare these values to those expected from the observed scaling relation between $L_{2500\,\text{Å}}$ and $\alpha_{ox}$ found by Just et al. (2007) for non-BAL QSOs,

$$\alpha_{OX} = (-0.140 \pm 0.007)\log(L_{2500\,\text{Å}}) + (2.705 \pm 0.212). \quad (25)$$

Taking the values of $L_{2500\,\text{Å}}$ for the two sightlines from our benchmark model, we obtain empirical predictions of $\alpha_{ox} = -1.66 \pm 0.43$ for $i = 40°$ and $\alpha_{ox} = -1.52 \pm 0.43$ for $i = 75°$. However, we still have to correct for the fact that BALQSOs are known to be X-ray weak (presumably due to absorption in the outflow). Gibson et al. (2009) find that the median $\Delta\alpha_{OX} = \alpha_{OX,BALQSO} - \alpha_{OX,QSO} = -0.17$ for all BALQSOs with BI $> 0$, but the distribution of $\Delta\alpha_{ox}$ is quite wide, and systems with large BI $\gtrsim 1000$ km s$^{-1}$ tend to have larger $\Delta\alpha_{ox}$. If we adopt $\Delta\alpha_{ox} \simeq -0.3$ as typical for strong BALQSOs (like our benchmark model), the empirically predicted value for the $i = 75°$ BALQSO sightline becomes $\alpha_{ox} \simeq -1.8 \pm 0.4$ (where the quoted uncertainty is purely that associated with the scaling relation for non-BAL QSOs).

These numbers make the X-ray weakness of the benchmark model clear: at fixed $L_{2500\,\text{Å}}$, the emergent X-ray flux predicted by the model is at least two orders of magnitude lower than the average observed values. Equivalently, the model corresponds to a 2–3$\sigma$ outlier in the $\alpha_{ox}$ distribution of (BAL)QSOs.

To investigate whether we can increase $L_X$ substantially while retaining the observed BAL features for sightlines looking into the wind cone, Fig. 11 shows the behaviour of the emergent spectra for $i = 75°$ and $i = 80°$ as the X-ray luminosity is increased from $L_X = 10^{43}$ erg s$^{-1}$ to $L_X = 10^{44}$ erg s$^{-1}$. We will focus on the behaviour of C IV and O VI as representative examples. For $i = 75°$, the C IV BAL feature becomes narrower with increasing $L_X$: it gradually disappears, starting from the blue edge. The feature is lost entirely by $L_X = 5 \times 10^{43}$ erg s$^{-1}$. The effect on the O VI feature is more abrupt, with almost no effect up to a luminosity of $3.7 \times 10^{43}$ erg s$^{-1}$, but complete disappearance for twice that luminosity. Similarly, for $i = 80°$, C IV weakens gradually in models with larger $L_X$, while in this case O VI shows hardly any response to $L_X$ until we reach $L_X = 10^{44}$ erg s$^{-1}$. Note that C IV is still present with a clear BAL signature at this X-ray luminosity for $i = 85°$.

The strong sensitivity of the UV resonance transition to $L_X$ in this range can be understood by considering the location of the photoionization edges for these species. Fig. 12 shows these locations
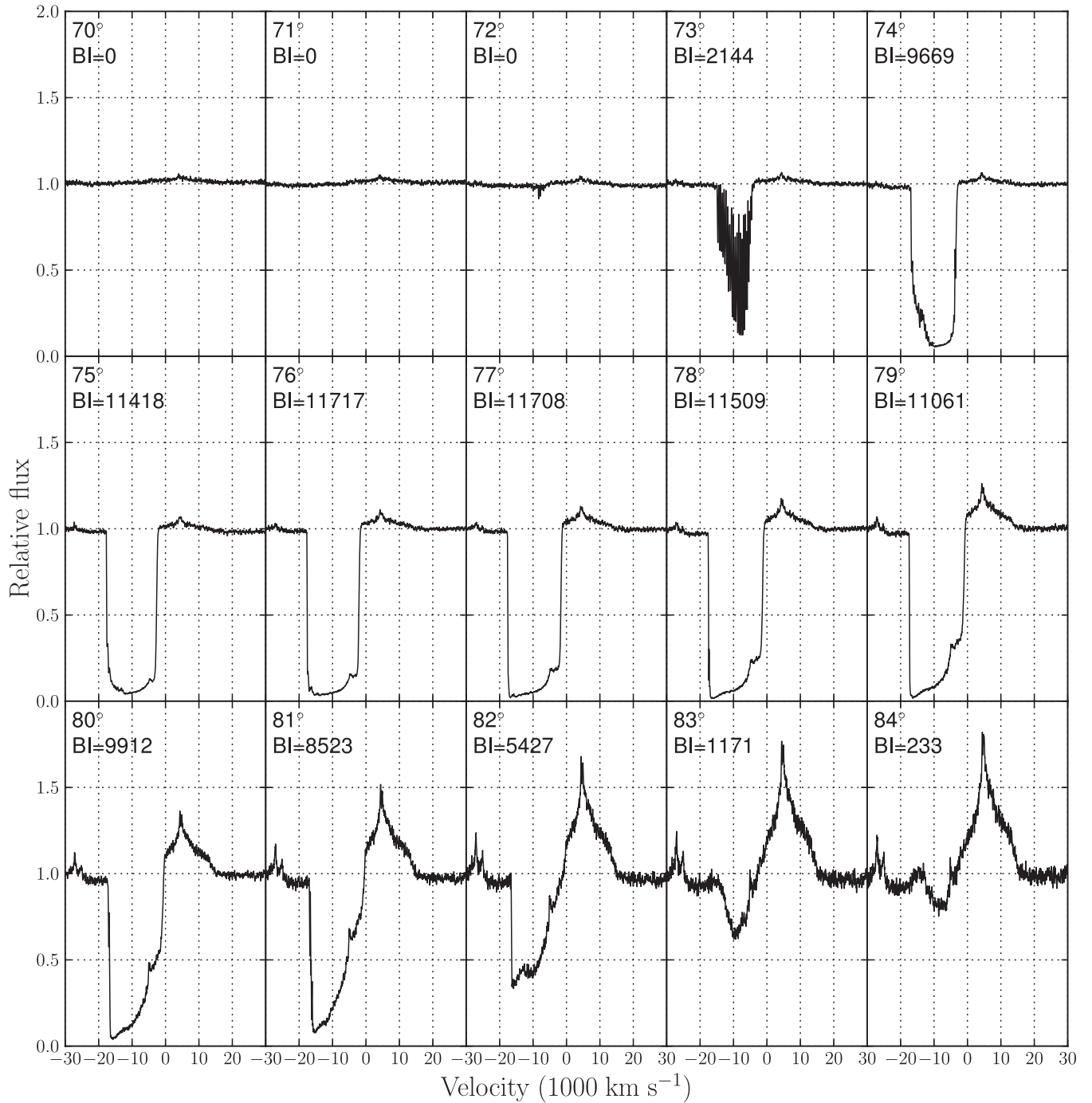
**Figure 9.** C IV line detail for sightlines between 70° and 84°. Each spectrum is scaled to a linear continuum, fitted at velocity ±30 000 km s⁻¹ The Balnicity Index for the spectrum is marked on each plot.

relative to the angle-averaged disc spectrum and the X-ray spectra corresponding to $L_X = 10^{43}$ erg s⁻¹ and $L_X = 10^{44}$ erg s⁻¹. The ionization edge of C IV falls very close to the frequency above which the X-ray source takes over from the disc as the dominant spectral component. In fact, for $L_X = 10^{43}$ erg s⁻¹, photoionization of C IV is driven primarily by disc photons, while for $L_X = 10^{44}$ erg s⁻¹, it is mainly due to photons from the X-ray source. The photoionization rate of higher ionization species like O VI is dominated by the X-ray source even at $L_X = 10^{43}$ erg s⁻¹.

We conclude that moderate increases in $L_X$ (by a factor of a few) would be feasible without any other parameter adjustments, but larger changes will begin to destroy BAL features for more and more sightlines. However, it is reasonable to anticipate that the negative effects of increasing $L_X$ on BAL features may be mitigated by simultaneously increasing the mass-loss rate in the wind, $\dot{M}_{\rm wind}$. We have therefore carried out a two-dimensional sensitivity study, in which we vary both $L_X$ and $\dot{M}_{\rm wind}$. The results – focusing particularly on the key C IV line profile for $i = 75°$ – are shown in Fig. 13. In each panel of this figure, we also give the BI measured for the profile shown, as well as values of $F/F_0$; the ratio of the continuum at $-30\,000$ km s⁻¹ to that obtained in a model without a wind.

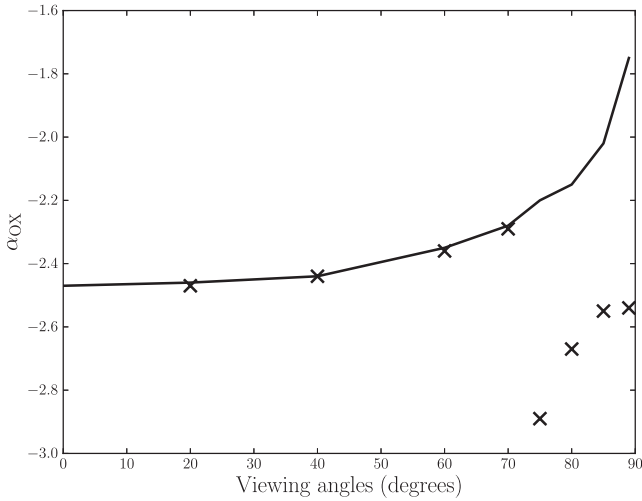**Figure 10.** Emergent $\alpha_{\text{ox}}$ values for benchmark model (symbols) and without wind (solid line).

The second column in Fig. 13 illustrates the effect of increasing $L_X$ while keeping the mass-loss rate at the benchmark value of $\dot{M}_{\text{wind}} = 5\,\text{M}_\odot\,\text{yr}^{-1}$ (as in Fig. 11). We see again that the C IV BAL feature persists up to at least $L_X = 10^{44}\,\text{erg s}^{-1}$, although it becomes both weaker and narrower with increasing $L_X$. For higher mass-loss rates (third and beyond columns in Fig. 13), the C IV profile becomes increasingly insensitive to $L_X$. So, as expected, increasing $\dot{M}_{\text{wind}}$ allows for the production of strong BAL features in species like C IV even at higher irradiating $L_X$. Thus, one way to address the

X-ray weakness of the benchmark model (i.e. increase $\alpha_{\text{ox}}$) is to increase both $L_X$ and $\dot{M}_{\text{wind}}$.

This remedy has a side effect: any increase in $\dot{M}_{\text{wind}}$ also implies an increase in $\tau_{\text{es}}$, the electron-scattering optical depth through the outflow. This reduces the *observed* X-ray and optical luminosity of the BALQSO. For moderate inclinations and mass-loss rates, the emergent continuum flux will scale simply as $e^{-\tau_{\text{es}}}$, although for the highest inclinations and $\dot{M}_{\text{wind}}$, scattered radiation will dominate the continuum and break this scaling. In any case, our main conclusion is that, for high mass-loss rates, we are able to produce BALs over a wider range of $L_X$ but at the expense of significant continuum suppression. If this is to provide a realistic route towards geometrical unification, it implies that the *intrinsic* luminosities of BALQSOs must be higher than suggested by their observed brightness.

There are, of course, other possibilities. For example, if the outflow is clumpy (e.g. Krolik, McKee & Tarter 1981; Arav et al. 1999), some of the X-ray radiation may pass through the wind unimpeded, thus increasing the observed $L_X$ for sightlines inside the wind cone. Such a solution would have the added advantage that the higher density within the clumps would naturally result in a lower ionization state for a given X-ray flux. Relaxing the assumption of a smooth flow would, of course, take us back in the direction of cloud models of the BLR and BALR. We plan to investigate the pros and cons of such scenarios in future work.

### 6.2 The weakness of line emission produced by the outflow

As mentioned in Section 5.2.2, our benchmark model does not produce strong emission line features, especially at low-inclination
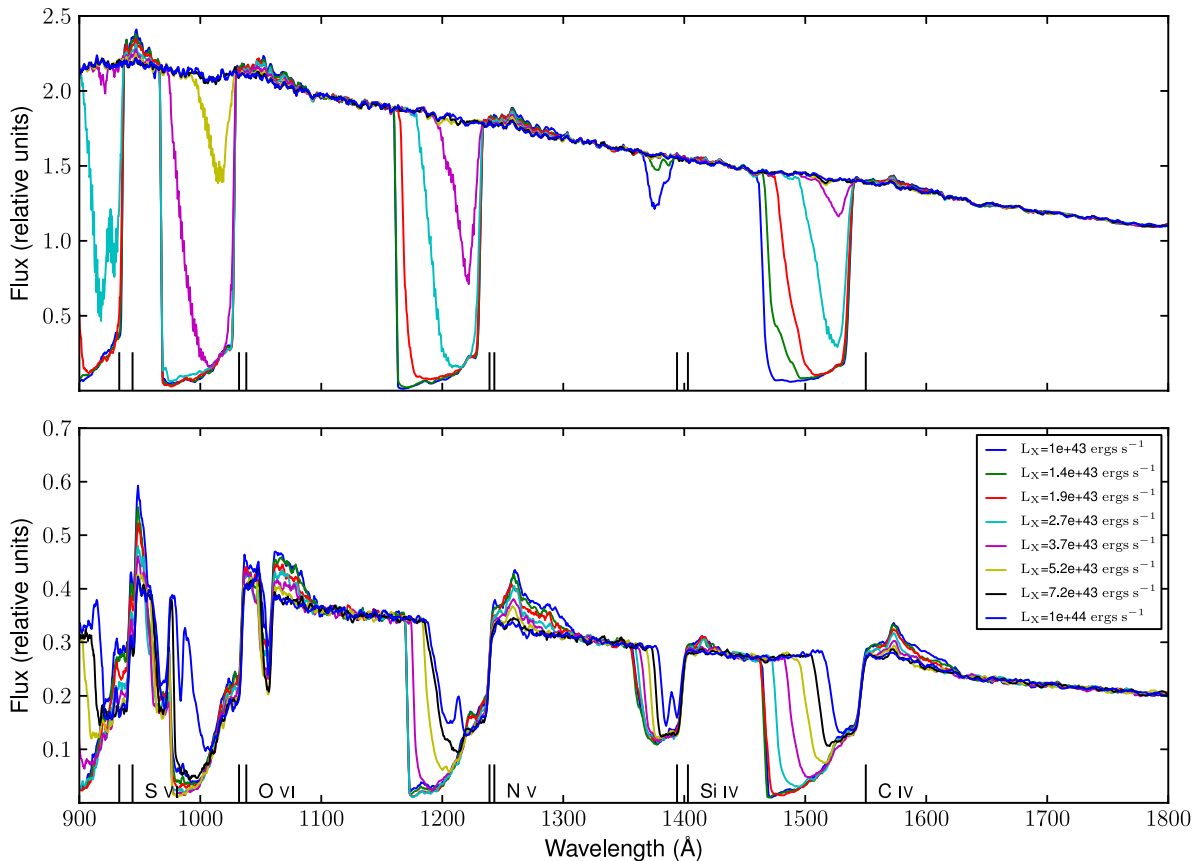


**Figure 11.** Spectra at $75°$ (top panel) and $80°$ sightlines for the benchmark model with a range of 2–10 keV luminosities.
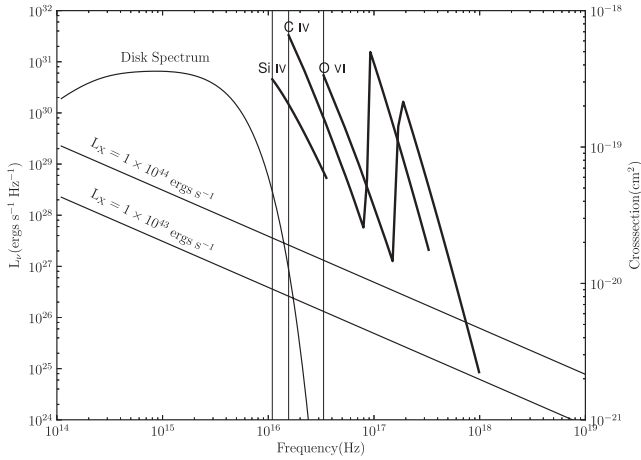
**Figure 12.** Input spectrum from the disc component in the benchmark model, together with the contribution from the central source for two different values of $L_X$. The photoionization cross-sections for C IV, O VI and Si IV are also plotted over the same frequency range.

models where the geometric unification scenario suggests Type I QSOs should be seen. This suggests that modifications are required in some aspect of the structure or the physics that is incorporated into PYTHON, if the geometric unification scenario is correct.

In considering this shortcoming, it is interesting to compare with the disc wind modelling carried out by Murray et al. 1995 (hereafter MCGV95). They explicitly model a line-driven outflow, and the broad characteristics of their disc wind are sufficiently similar to our benchmark model to make a comparison interesting. MCGV find that their outflow produces BAL troughs when viewed at high inclinations. However, they also find that their model produces sufficient collisionally excited emission in species like C IV to explain the BEL in both BALQSOs and non-BAL QSOs. In their model, this C IV emission arises in a layer of the wind close to the disc plane where C IV is the dominant ionization stage of carbon. They argue that this region extends from $\simeq 10^{16}$ cm to $\simeq 10^{17}$ cm and is characterized by $T_e \simeq 20\,000$ K and $n_e \simeq 10^{10}$ cm$^{-3}$. It is the integrated, collisionally excited emission from this region that dominates the C IV line flux in their model.

In the case of our benchmark model, Fig. 5 shows that the fractional C IV abundance is high ($f_{\text{C IV}} \gtrsim 0.1$) in a region extending from $x \simeq 5 \times 10^{16}$ cm to $x \simeq 3 \times 10^{17}$ cm. However, the density in this region is considerably lower than in the C IV line-forming region considered by MCGV: $10^7$ cm$^{-3} \lesssim n_e \lesssim 10^9$ cm$^{-3}$. It is this lower density that almost certainly explains the difference in C IV emissivity in the models. In a later version of their model (Murray & Chiang 1998), the production of C IV is dominated by lower density ($n_e \simeq 10^8$ cm$^{-3}$) material lying at larger radii $r \gtrsim 10^{18}$ cm. In these models, it is the large emitting volume that explains the strength of collisionally excited C IV feature.

These comparisons suggest that moderate changes to the benchmark model may be enough to produce BELs via collisionally excited line emission in the outflow. It is likely that such changes would go in the direction of increasing the density in some parts of the wind, either by modifying existing wind parameters or by introducing clumpiness. In fact, we can clearly see that the emission component of the C IV line in Fig. 13 does increase with increasing $\dot{M}_{\text{wind}}$. However, even our highest $\dot{M}_{\text{wind}}$ models do not yet produce enough emission at low inclination angles. Thus, while the benchmark model shows some promise in the context of geometric unification, it remains to be seen whether (and how) it can be mod-

ified to produce the strong emission lines seen in both BALQSOs and non-BAL QSOs. This will be the subject of a separate paper.

Before we leave this section, it is interesting to ask why the *scattering* of C IV photons in the outflow does not produce emission lines of sufficient strength in our model. In CV winds, for example, modelling suggests that resonance scattering is the primary mechanism for producing the observed emission line profiles (SV93; Knigge et al. 1995; LK02; Noebauer et al. 2010). The critical factor in understanding the relative importance of scattered photons to the line formation process is the combination of foreshortening, limb-darkening, outflow orientation and covering factor. The outflows in CVs are thought to be ejected roughly perpendicular to the accretion disc, albeit over quite a large range of opening angles. Moreover, CV winds emerge directly above the continuum emitting regions of the disc, whereas BALQSO winds cover only $\simeq 20$ per cent as seen from the continuum source. Thus, in a CV, an outflow that is optically thick in C IV over some velocity interval will intercept virtually all of the continuum photons within this interval – and scatter them into other sightlines, where they emerge as apparent line emission. Conversely, our QSO wind scatters only a small fraction of the continuum photons, even in frequency intervals in which the wind is optically thick. As a result, scattered photons will not contribute as much to emission line formation.

### 6.3 Ionization stratification and reverberation mapping

In our benchmark model, the ionization state of the outflow tends to increase with increasing distance along poloidal streamlines (Fig. 5). This is easily understood. Far away from the central engine, in the region of the flow where the BAL features are produced, the wind geometry approximates an optically thin, spherical outflow. In such an outflow, $U \propto v(r)$, so as long as the wind accelerates, the ionization parameter must also increase outwards.

This trend may appear to contradict reverberation mapping studies of the BLR, which suggest ionization stratification in the opposite sense. For example, the C IV BLR radius at fixed UV luminosity inferred by Kaspi et al. (2007) is $\simeq$ two times smaller than that obtained by Kaspi et al. (2005) for H$\beta$. This sense of ionization stratification is also supported by recent microlensing results (e.g. Guerras et al. 2013).

However, our model is not necessarily in conflict with these empirical findings. As discussed in Section 6.2, it is clear that the parts of the wind producing BALs (where $U$ increases outwards) are unlikely to be co-spatial with the parts of the wind producing BELs. More specifically, only the dense base of the disc wind is likely to produce significant amounts of collisionally excited line emission. Thus, in the context of disc wind models, the reverberation mapping results are unlikely to probe the 'radial' ionization structure of the outflow, but may instead probe the stratification along the base of the wind in the $x$ direction. Here, the ionization parameter can (and does) decrease outwards in our disc wind models.

### 6.4 Implications

Here we consider implications of our benchmark model for AGN feedback in galaxy evolution and identifying possible driving mechanisms for the wind.

In energetic terms, effective feedback – sufficient to establish the $M_{\text{BH}}-\sigma$ relation, for example – seems to require $L_k/L_{\text{bol}} \simeq 0.005$–$0.05$ (Di Matteo, Springel & Hernquist 2005; Hopkins & Elvis 2010). Here, $L_k = \frac{1}{2}\dot{M}_{\text{wind}}v_\infty^2$ is the kinetic luminosity of the outflow. Our benchmark model is characterized by
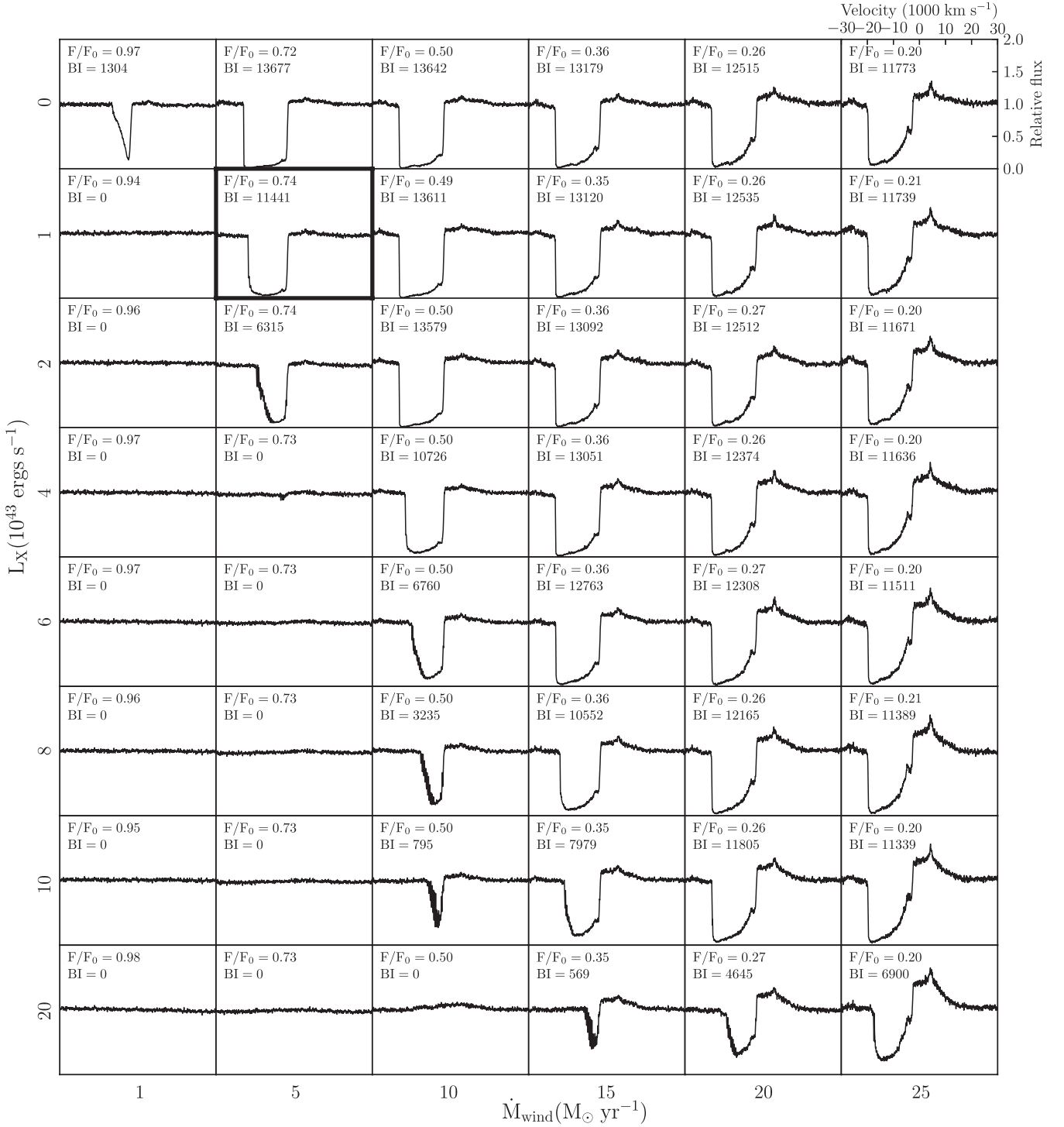
**Figure 13.** Spectrum detail around the C IV line feature for the benchmark model and others with a range of X-ray luminosity and $\dot{M}_{\rm wind}$. Spectra are all for $i = 75°$ and are normalized to a linear continuum model fitted at $\pm 30\,000\,\mathrm{km\,s^{-1}}$. Values of $F/F_0$ show the ratio of the continuum at $-30\,000\,\mathrm{km\,s^{-1}}$ to that obtained in a model without a wind. The scales for each sub-plot are given on the upper right-hand sub-plot and the baseline model is highlighted.

$v_\infty \simeq 20\,000\,\mathrm{km\,s^{-1}}$ and $\dot{M}_{\rm wind} = 5\,\mathrm{M_\odot\,yr^{-1}}$, which yields $L_k/L_{\rm bol} \simeq 0.025$. Thus, an outflow of this type would be capable of providing significant amounts of energy-driven feedback. The kinetic luminosity of the benchmark model is also broadly in line with the empirical scaling between $L_{\rm bol}$ and $L_k$ found by King et al. (2013) for black holes across the entire mass-scale, from compact binary systems to AGN/QSO.

King (2003, 2005, 2010) has argued that QSO outflows interact with their host galaxy in a *momentum*, rather than energy-driven fashion. In this case, the strength of the feedback an outflow can deliver depends on its momentum flux, $\dot{M}_{\rm wind} v_\infty$. This scenario naturally produces the observed $M_{\rm BH}-\sigma$ relation if the outflows responsible for feedback satisfy $\dot{M}_{\rm wind} v_\infty \simeq L_{\rm Edd}/c$; this is the single-scattering limit for momentum transfer in a radiatively driven

outflow from a QSO radiating at $L_{edd}$. For our benchmark model, we find $\dot{M}_{wind}v_\infty \simeq 0.7L_{bol}/c \simeq 0.1L_{Edd}/c$. In other words, the momentum flux in our model is close to the single-scattering limit for its bolometric luminosity. Since black hole growth and cosmological feedback are thought to be dominated by phases in which $L_{bol} \simeq L_{Edd}$ (Soltan 1982; Yu & Tremaine 2002; Di Matteo et al. 2005), outflows of this type would probably also meet momentum-based feedback requirements.

The momentum flux in the outflow is also a key parameter for any disc wind driven by radiation pressure, such as the line-driven winds considered by MCGV95 and Proga et al. (2000). In particular, such winds typically satisfy the single-scattering limit for momentum transfer from the radiation field to the outflow, $\dot{M}_{wind}v_\infty \leq L_{bol}/c$. As noted above, our benchmark model also satisfies this limit. However, this is somewhat misleading: our disc wind subtends only $\simeq 20$ per cent of the sky as seen from the central source, and it intercepts an even smaller fraction of the QSOs bolometric luminosity (due to foreshortening and limb-darkening of the disc radiation field). The momentum flux in our benchmark model actually exceeds the single-scattering limit if only momentum carried by photons that actually intercept the wind is taken into account. Thus, in the context of radiatively driven winds, either the mass-loss rate in our model must be overestimated or multiple scattering effects must be important. The latter has been suggested for quasi-spherical Wolf–Rayet star winds (Lucy & Abbott 1993; Springmann 1994; Gayley 1995) but is much more challenging for the biconical wind considered here. Alternatively, the winds of QSOs may not be driven (exclusively) by radiation pressure, with magnetic/centrifugal forces providing the most obvious alternative (e.g. Blandford & Payne 1982; Emmering, Blandford & Shlosman 1992; Proga 2003).

Our discussion of all these considerations is preliminary: the benchmark model is far from perfect, and we have not yet carried out a comprehensive survey of the available parameter space. However, the first column in Fig. 13 shows that a reduction in the mass-loss rate from the benchmark value of $\dot{M}_{wind} = 5M_\odot$ yr$^{-1}$ to $\dot{M}_{wind} = 1M_\odot$ yr$^{-1}$ virtually destroys the BAL features, even for $L_X = 10^{43}$ erg s$^{-1}$. Thus, at least for our adopted wind geometry and kinematics, it seems that any outflow capable of producing BAL features is also likely to provide significant feedback and pose a challenge to line-driving.

### 6.5 Outlook

In our view, the most significant shortcomings of the benchmark model are its intrinsic X-ray weakness and its inability to produce collisionally excited BELs. Both problems might be resolved by moderate changes in wind parameters, so an important step will be to explore the parameter space of our model. We plan to adopt two complementary approaches in this: (i) systematic grid searches; (ii) targeted explorations guided by physical insight. The latter approach is important, since compromises will have to be made in the former: a detailed and exhaustive search over all relevant parameters is likely to be prohibitive in terms of computational resource requirements. As an example of how physical insight can guide us, we note that both the X-ray and emission line problems might be resolved by increasing the density in specific wind regions.

### 7 SUMMARY

This paper represents the first step in a long-term project to shed light on the nature of accretion disc winds in QSOs. These outflows

may be key to the geometric unification of AGN/QSO and might also provide the feedback required by successful galaxy evolution scenarios.

In this pilot study, we have focused on the most obvious signature of these outflows, the broad, blue-shifted absorption lines seen in $\simeq 20$ per cent of QSOs. We have constructed a kinematic disc wind model to test if it can reproduce these features. This benchmark model describes a rotating, equatorial and biconical accretion disc wind with a mass-loss rate $\dot{M}_{wind} \simeq \dot{M}_{acc}$.[5] A Monte Carlo ionization and radiative transfer code, PYTHON, was used to calculate the ionization state of the outflow and predict the spectra emerging from it for a variety of viewing angles. Our main results are as follows.

(i) Our benchmark model succeeds in producing BAL-like features for sightlines towards the central source that lie fully within the wind cone.

(ii) Self-consistent treatment of ionization and radiative transfer is necessary to reliably predict the ionization state of the wind and the conditions under which key species like C IV can efficiently form.

(iii) The benchmark model does not produce sufficient collisionally excited line emission to explain the BELs in QSOs. However, we argue that moderate modifications to its parameters might be sufficient to remedy this shortcoming.

(iv) The ionization structure of the model, and its ability to produce BALs, are quite sensitive to the X-ray luminosity of the central source. If this is too high, the wind becomes overionized. In our benchmark model, $L_X$ is arguably lower than indicated by observations. Higher values of $L_X$ may require higher outflow columns – e.g. via higher $\dot{M}_{wind}$ – in order to still produce BALs.

(v) For our adopted geometry and kinematics, $\dot{M}_{wind} \gtrsim \dot{M}_{acc}$ is required in order to produce significant BAL features. The kinetic luminosity and momentum carried by such outflows is sufficient to provide significant feedback.

### REFERENCES

Abbot D. C., Lucy L. B., 1985, ApJ, 288, 679
Allen J. T., Hewett P. C., Maddox N., Richards G. T., Belokurov V., 2011, MNRAS, 410, 860
Arav N., 1996, ApJ, 465, 617
Arav N., Korista K. T., Barlow T. A., Begelman M. C., 1995, Nat, 376, 576
Arav N., Korista K. T., de Kool M., Junkkarinen V. T., Begelman M. C., 1999, ApJ, 516, 27
Arav N., Moe M., Costantini E., Korista K. T., Benn C., Ellison S., 2008, ApJ, 681, 954
Badnell N. R., 2006, ApJS, 167, 334
Becker R. H., White R. L., Gregg M. D., Brotherton M. S., Laurent-Muehleisen S. A., Arav N., 2000, ApJ, 538, 72
Begelman M. C., Blandford R. D., Rees M. J., 1984, Rev. Mod. Phys., 56, 255

---

[5] Strictly speaking, this is not entirely self-consistent, since the presence of such an outflow would alter the disc's temperature structure. However, we neglect this complication, since the vast majority of the disc luminosity arises from well within our assumed wind-launching radius.

Blandford R. D., Payne D. G., 1982, MNRAS, 199, 883

Blundell K. M., Mioduszewski A. J., Muxlow T. W. B., Podsiadlowski P., Rupen M. P., 2001, ApJ, 562, L79

Borguet B., Hutsemékers D., 2010, A&A, 515, A22

Bottorff M., Korista K. T., Shlosman I., Blandford R. D., 1997, ApJ, 479, 200

Brotherton M. S., De Breuck C., Schaefer J. J., 2006, MNRAS, 372, L58

Capellupo D. M., Hamann F., Shields J. C., Rodríguez Hidalgo P., Barlow T. A., 2011, MNRAS, 413, 908

Capellupo D. M., Hamann F., Shields J. C., Rodríguez Hidalgo P., Barlow T. A., 2012, MNRAS, 422, 3249

Capellupo D. M., Hamann F., Shields J. C., Halpern J. P., Barlow T. A., 2013, MNRAS, 429, 1872

Cordova F. A., Mason K. O., 1982, ApJ, 260, 716

Cottis C. E., Goad M. R., Knigge C., Scaringi S., 2010, MNRAS, 406, 2094

Cunto W., Mendoza C., Ochsenbein F., Zeippen C. J., 1993, A&A, 275, L5

Dere K. P., Landi E., Mason H. E., Monsignori Fossi B. C., Young P. R., 1997, A&AS, 125, 149

Di Matteo T., Springel V., Hernquist L., 2005, Nat, 433, 604

Done C., Davis S. W., Jin C., Blaes O., Ward M., 2012, MNRAS, 420, 1848

Elvis M., 2000, ApJ, 545, 63

Elvis M., Risaliti G., 2010, A&A, 516A, 89

Emmering R. T., Blandford R. D., Shlosman I., 1992, ApJ, 385, 460

Everett J. E., Königl A., Kartje J. F., 2001, ASP Conf. Ser. Vol. 224, Probing the Physics of Active Galactic Nuclei. Astron. Soc. Pac., San Francisco, p. 441

Everett J., Königl A., Arav N., 2002, ApJ, 569, 617

Fabian A. C., 2012, ARA&A, 50, 455

Fender R., 2006, in Lewin W. H. G., van der Klis M., eds, Compact stellar X-ray sources. Cambridge Univ. Press, Cambridge, p. 381

Ferland G. J., 2011, Hazy, A Brief Introduction to cloudy C10. Univ. Kentucky, Lexington

Ferland G. J. et al., 2013, Rev. Mexicana Astron. Astrofis., 49, 137

Galeev A. A., Rosner R., Vaiana G. S., 1979, ApJ, 229, 318

Ganguly R., Brotherton M. S., 2008, ApJ, 672, 102

Ganguly R., Sembach K. R., Tripp T. M., Savage B. D., Wakker B. P., 2006, ApJ, 645, 868

Gayley K. G., 1995, ApJ, 454, 410

Gibson R. R. et al., 2009, ApJ, 692, 758

Giustini M., Proga D., 2012, ApJ, 758, 70

Giustini M., Cappi M., Vignali C., 2008, A&A, 491, 425

Granato G. L., Silva L., Monaco P., Panuzzo P., Salucci P., De Zotti G., Danese L., 2001, MNRAS, 324, 757

Greenstein J. L., Oke J. B., 1982, ApJ, 258, 209

Guerras E., Mediavilla E., Jimenez-Vicente J., Kochanek C. S., Muñoz J. A., Falco E., Motta V., 2013, ApJ, 764, 160

Hewett P. C., Foltz C. B., 2003, AJ, 125, 1784

Hopkins P. F., Elvis M., 2010, MNRAS, 401, 7

Just D. W., Brandt W. N., Shemmer O., Steffen A. T., Schneider D. P., Chartas G., Garmire G. P., 2007, ApJ, 665, 1004

Kaspi S., Smith P. S., Netzer H., Maoz D., Jannuzi B. T., Giveon U., 2000, ApJ, 533, 631

Kaspi S., Maoz D., Netzer H., Peterson B. M., Vestergaard M., Jannuzi B. T., 2005, ApJ, 629, 61

Kaspi S., Brandt W. N., Maoz D., Netzer H., Schneider D. P., Shemmer O., 2007, ApJ, 659, 997

Kellermann K. I., Sramek R., Schmidt M., Shaffer D. B., Green R., 1989, AJ, 98, 1195

King A., 2003, ApJ, 596, L27

King A., 2005, ApJ, 635, L121

King A. R., 2010, MNRAS, 402, 1516

King A. L. et al., 2013, ApJ, 762, 103

Knigge C., 1999, MNRAS, 309, 409

Knigge C., Woods J. A., Drew J. E., 1995, MNRAS, 273, 225

Knigge C., Scaringi S., Goad M. R., Cottis C. E., 2008, MNRAS, 386, 1426

Körding E. G., Knigge C., Tzioumis T., Fender R., 2011, MNRAS, 418, L129

Krolik J. H., Voit G. M., 1998, ApJ, 497, L5

Krolik J. H., McKee C. F., Tarter C. B., 1981, ApJ, 249, 422

Lada C. J., 1985, ARA&A, 23, 267

Landi E., Del Zanna G., Young P. R., Dere K. P., Mason H. E., 2012, ApJ, 744, 99

Long K. S., Knigge C., 2002, ApJ, 579, 725 (LK02)

Lucy L. B., 1999, A&A, 345, 211

Lucy L. B., Abbott D. C., 1993, ApJ, 405, 738

Marsh T. R., Horne K., 1988, MNRAS, 235, 269

McNamara B. R., Nulsen P. E. J., 2007, ARA&A, 45, 117

Morton D. C., 1967, ApJ, 150, 535

Murray N., Chiang J., 1996, Nat, 382, 789

Murray N., Chiang J., 1998, ApJ, 494, 125

Murray N., Chiang J., Grossman S. A., Voit G. M., 1995, ApJ, 451, 498 (MCGV95)

Neilsen J., Lee J. C., 2009, Nat, 458, 481

Noebauer U. M., Long K. S., Sim S. A., Knigge C., 2010, ApJ, 719, 1932

North M., Knigge C., Goad M., 2006, MNRAS, 365, 1057

Ogle P. M., Cohen M. H., Miller J. S., Tran H. D., Goodrich R. W., Martel A. R., 1999, ApJS, 125, 1

Ponti G., Fender R. P., Begelman M. C., Dunn R. J. H., Neilsen J., Coriat M., 2012, MNRAS, 422, L11

Proga D., 2003, ApJ, 585, 406

Proga D., Kallman T. R., 2004, ApJ, 616, 688

Proga D., Stone J. M., Kallman T. R., 2000, ApJ, 543, 686

Reichard T. A. et al., 2003, AJ, 126, 2594

Schawinski K., Thomas D., Sarzi M., Maraston C., Kaviraj S., Joo S. J., Yi S. K., Silk J., 2007, MNRAS, 382, 1415

Schurch N. J., Done C., 2007, MNRAS, 381, 1413

Schurch N. J., Done C., Proga D., 2009, ApJ, 694, 1

Shakura N. I., Sunyaev R. A., 1973, A&A, 24, 337

Shlosman I., Vitello P., 1993, ApJ, 409, 372 (SV93)

Sim S. A., 2005, MNRAS, 356, 531

Sim S. A., Drew J. E., Long K. S., 2005, MNRAS, 363, 615

Sim S. A., Long K. S., Miller L., Turner T. J., 2008, MNRAS, 388, 611S

Sim S. A., Miller L., Long K. S., Turner T. J., 2010, MNRAS, 404, 1369

Simon L. E., Hamann F., 2010, MNRAS, 409, 269

Smak J., 1981, Acta Astron., 31, 395

Soltan A., 1981, MNRAS, 200, 115

Springmann U., 1994, A&A, 289, 505

Sutherland R. S., 1998, MNRAS, 300, 321S

Treister E., Urry C. M., Virani S., 2009, ApJ, 696, 110

Turner T. J., Miller L., 2009, A&AR, 17, 47

Verner D. A., Barthel P. D., Tytler D., 1994, A&A, 108, 287

Verner D. A., Ferland G. J., Korista K. T., Yakovlev D. G., 1996, ApJ, 465, 487

Verner D. A., Verner E. M., Ferland G. J., 1996, At. Data Nucl. Data Tables, 64, 1

Weyman R. J., Morris S. L., Foltz C. B., Hewitt P. C., 1991, ApJ, 373, 23

Xu Y., Bian W. H., Yuan Q. R., Huang K. L., 2008, MNRAS, 389, 1703

Yu Q., Tremaine S., 2002, MNRAS, 335, 965

Zhou H., Wang T., Wang H., Wang J., Yuan W., Lu Y., 2006, ApJ, 639, 716

This paper has been typeset from a TEX/LATEX file prepared by the author.